Microstructure and fracture toughness characterization of three 9Cr ODS EUROFER steels with different thermo-mechanical treatments

Das, A.; Chekhonin, P.; Altstadt, E.; Mcclintock, D.; Bergner, F.; Heintze, C.; Lindau, R.;

Originally published:

August 2020

Journal of Nuclear Materials 542(2020), 152464

DOI: https://doi.org/10.1016/j.jnucmat.2020.152464

Microstructure and fracture toughness characterization of three 9Cr ODS EUROFER steels with different thermo-mechanical treatments

A. Das[1,a,b] , P. Chekhonin[a], E. Altstadt[a] , D. McClintock[c], F. Bergner[a], C. Heintze[a], R. Lindau[d]

[a] Helmholtz-Zentrum Dresden-Rossendorf, Bautzner Landstrasse 400, 01328 Dresden, Germany

[b] Chair of Radiochemistry/Radioecology, Technische Universität Dresden, 01062 Dresden, Germany

[c] Oak Ridge National Laboratory, Oak Ridge, TN, USA

[d] Institute for Applied Materials, Karlsruhe Institute of Technology, Hermann-von-Helmholtz-Platz 1, 76344 Eggenstein-Leopoldshafen, Germany

[1] Corresponding author, e-mail: a.das@hzdr.de

Abstract

Ferritic martensitic ODS steels are one of the candidate structural materials for future Gen-IV nuclear fission and fusion reactors. The dependence of fracture toughness on microstructure was investigated by comparing three 9Cr ODS EUROFER steels manufactured through different thermo-mechanical processing routes. Quasi-static fracture toughness testing was performed with sub-sized C(T) specimens and microstructural characterization was carried out using scanning electron microscopy, electron backscatter diffraction, and transmission electron microscopy. It was found that at lower test temperatures (-100 to 22 °C), the fracture toughness was primarily controlled by crack initiation at sub-micron particles and by production of secondary cracks during fracture. At higher temperatures (above 100 °C), fracture toughness was predominantly controlled by the matrix ductility and the grain boundary strength with a relatively ductile coarse-grained alloy demonstrating higher fracture toughness compared to high-strength fine-grained alloys. These results and discussion show that variations in thermomechanical treatments can produce significant differences in microstructure and fracture toughness behaviour of ferritic martensitic ODS steels.

Keywords

ODS steel, ferritic martensitic alloys, microstructure characterization, fracture toughness, structure-property relationship

Highlights

- Three 9Cr ODS EUROFER steels are compared with respect to microstructure and fracture toughness
- Secondary cracking induced by residual ferrite improves fracture toughness at lower temperatures
- Matrix ductility predominantly controls the fracture toughness at temperatures between 100 ˚C and 500 ˚C
- Above 500 ˚C, the grain boundary strength predominantly controls the fracture toughness
- Variations in thermo-mechanical history lead to significant differences in microstructure and fracture behaviour

1 Introduction

Systematic development of reduced activation ferritic-martensitic (RAFM) steels as structural material for nuclear applications in Europe resulted in several alloys, one of which was the 9% CrWVTa alloy EUROFER [1]. This alloy exhibited good resistance against irradiation induced swelling and high-temperature creep and was capable of withstanding operating temperatures up to 550 ˚C [2]. In order to increase the capability of the material to withstand operating temperatures up to 650 ˚C and to further improve its high-temperature creep strength and resistance towards irradiation induced effects, oxide particles were dispersed in the microstructure. This variant came to be known as oxide dispersion strengthened (ODS) EUROFER. In general, ferritic martensitic ODS steels with 9-12 wt.% Cr, like ODS EUROFER, are considered as candidate materials for blankets in fusion reactors [3–20]. ODS EUROFER batches were manufactured via different thermo-mechanical routes and hence developed slight variations in microstructure. The fracture toughness is directly related to the microstructure, and is an extremely important parameter affecting the loading capacity, machinability and formability of a material [21,22]. Therefore it becomes important to study the impact of variation in microstructure on the fracture toughness of 9Cr ODS EUROFER steels.

The initial mechanically alloyed and hot isostatic pressed version of ODS EUROFER was known as “first generation ODS EUROFER”. It exhibited good tensile and creep properties but poor impact properties [3,8,14]. The second generation ODS EUROFER, which was developed through optimization of hot-rolling and thermo-mechanical treatments, exhibited comparable tensile and creep strength, and higher fracture toughness as compared to the first generation ODS EUROFER [1,3]. Later, a new version of ODS EUROFER, denominated “EU batch”, was developed. This batch exhibited somewhat lower fracture toughness than the second generation ODS EUROFER but significantly higher than the first generation ODS EUROFER [3,8]. Still later, the heat treatment of the “EU batch” was modified by replacing the water quenching performed directly after the austenitization with air cooling.

The mechanical properties of these ODS EUROFER steels alongside with some microstructural data have been reported in several previous publications [3,9,11,15,18,23,24]. However, regarding the newer ODS EUROFER batches (i.e. second generation and the EU batch), it remains unclear how changes in thermo-mechanical treatment explain differences in fracture properties. In order to improve this understanding, in the present work, three non-irradiated ODS EUROFER steels with similar composition but different thermo-mechanical treatment were compared with respect to their microstructure and fracture toughness.

Fracture toughness testing was performed by sub-sized compact tension specimens (0.25T C(T)) in the temperature range of -100 ˚C to 600 ˚C and detailed microstructural characterisation was performed by means of scanning electron microscopy (SEM), electron backscatter diffraction (EBSD) and transmission electron microscopy (TEM). In this work, we highlight how fracture toughness is affected by microstructural variations resulting from different thermo-mechanical processing.

2 Materials and methods

2.1 Materials

The nominal composition of EUROFER, the European reference RAFM steel, is (wt.%) 8.9Cr, 1.1W, 0.2V, 0.14Ta, 0.42Mn, 0.06Si, 0.11C and Fe for the balance [14]. Second generation ODS EUROFER was produced in cooperation between Karlsruhe Institute of Technology (KIT), Germany, and Plansee. Some of this material was sent to Oak Ridge National Laboratory (ORNL) in the USA for irradiation in the High Flux Isotope Reactor (HFIR) and testing [15]. The present investigation on second generation ODS EUROFER is based on the material provided by D. McClintock from ORNL to Helmholtz-Zentrum Dresden-Rossendorf (HZDR). The production route involved mechanical alloying (MA) of steel powder with 0.3% Y_2O_3 followed by compaction using hot isostatic pressing (HIP). After this, the material was thermo-mechanically treated including hot-rolling (HR) at 1150 ˚C and then cooling to room temperature (RT) followed by re-austenitization at 1100 ˚C for 30 min with water quenching to RT and tempering at 750 ˚C for 2 h [3,9,15,18]. This material is designated herein as “ODS_WQ_RT”.

The EU batch was produced by Plansee and subsequently delivered to KIT in the form of 6 mm thick hot-rolled plate. Some material was also provided to the Belgium nuclear research center SCK-CEN. A small piece of this material was provided by R. Chaouadi (SCK-CEN) to HZDR for microstructural investigations. This material is designated herein as “ODS_WQ_450”. The thermo-mechanical processing history of ODS_WQ_450 was similar to ODS_WQ_RT except that the water quenching after the austenitization process ended at 450 ˚C [3,23].

A slightly different version of ODS_WQ_RT, designated herein as ODS_AC_RT, was provided by R. Lindau (KIT) to HZDR. Here, after the austenitization step at 1100 ˚C, the 6 mm thick plate was air cooled instead of water quenched to RT. Even though the material was not water quenched, the cooling rate was still high enough for martensite formation. The details of the manufacturing processes for all the three ODS EUROFER materials in this work are compiled in Table 1. The composition of ODS_AC_RT is presented in Table 2 which is similar to the other two ODS EUROFER batches.

Table 1 Manufacturing methods and heat treatments of the three ODS EUROFER batches

Batch Name	Manufacturing Method and Heat Treatments	References
ODS_WQ_450	MA + HIP + HR 1150 ˚C + austenitization 1100 ˚C/30 mins + water quenching to 450 ˚C + tempering 750 ˚C/2 h	[3,23]
ODS_WQ_RT	MA + HIP + HR 1150 ˚C + austenitization 1100 ˚C/30 mins + water quenching to RT + tempering 750 ˚C/2 h	[3,9,15,18]
ODS_AC_RT	MA + HIP + HR 1150 ˚C + austenitization 1100 ˚C/30 mins + air cooling to RT + tempering 750 ˚C/2 h	[25]

Table 2 Composition of ODS and non-ODS EUROFER steels

Wt. %	Cr	W	V	Ta	Mn	Si	C	Fe	Y_2O_3
ODS_WQ_450 [23]	8.9	1.11	0.19	0.08	0.41	0.11	0.07	bal.	0.3
ODS_WQ_RT [18]	9	1	0.2	0.1	0.44	0.1	0.07	bal.	0.3
ODS_AC_RT	9.2	1.14	0.19	0.03	0.38	0.03	0.086	bal.	0.312
9% CrWVTa EUROFER [23]	9	1.1	0.19	0.13	0.44	0.07	0.12	bal.	-

2.2 Microscopy

Microstructure characterization

Optical microscopy (Leica REICHERT MEF4) was used to investigate the inhomogeneities in the microstructure. The samples were etched using the following procedure: ODS_WQ_450 for 6 minutes using 5% HNO_3, ODS_WQ_RT for approximately 30 seconds in 50 ml distilled water + 15 ml hydrochloric acid + 2.5 g iron (III) chloride and ODS_AC_RT for 10 minutes in picric acid with ammonia washout. SEM was then used to investigate the bulk microstructure, especially with respect to the bigger sub-micron particles; a Zeiss EVO 50 SEM equipped with a tungsten electron cathode was used for secondary electron (SE) imaging. The samples for SEM investigations were etched similarly like for optical microscopy except ODS_AC_RT, which was etched for approximately 30 seconds using 50 ml distilled water, 15 ml hydrochloric acid and 2.5 g iron (III) chloride.

To reveal the grain structure, samples were characterized via EBSD with a Zeiss NVision 40 CrossBeam (Focused ion beam (FIB) and SEM) equipped with a field emission electron cathode and a Bruker EBSD acquisition system with an e- Flash HR+ detector. Sample surface preparation for EBSD included grinding on wet SiC paper and (as final step) mechanical polishing with an oxide polishing suspension (OP-S) consisting of amorphous silica, water and 1,3-butanediol. All EBSD measurements were done using an acceleration voltage of 15 kV and a step size of 80 nm resulting in indexation rates of at least 95%.

For EBSD data evaluation, an EBSD software developed at HZDR was used which corrects outliers and unindexed points (down to five indexed neighbours) and facilitates advanced analyses such as discrimination by grain size. Since high-angle grain boundaries (HAGBs) as opposed to low-angle grain boundaries (LAGBs) generally play a dominant role in fracture [26], the misorientation angle for grain reconstruction was arbitrarily set to 10° for all three ODS alloys. Only grains consisting of 5 or more mapping pixels (corresponding to an equivalent diameter d of 0.2 µm) were considered in the evaluation. Subsequently, the reconstructed grains were subdivided into ultra-fine grains (defined here as $d \leq 1$ µm) and coarse grains ($d > 1$ µm).

To obtain details on all included particles, TEM investigations were performed using a Talos F200X FEG-(S) TEM (FEI) with 200 keV acceleration voltage. For all three ODS steels, thin 3 mm disks were electro-polished with a TenuPol-5 (Struers) in 5% perchloric acid in methanol at -60 °C applying a polishing voltage of 23 V. Sub-micron particles were visualized by scanning transmission electron microscope (STEM) imaging in combination with a high-angle annular dark-field (HAADF) detector and analysed by energy-dispersive X-ray spectroscopy (EDX). Thickness determination was done via convergent beam electron diffraction (CBED) using a comparison between experimental and simulated CBED patterns obtained by the software TEMStrain by A. Morawiec [27]. Additionally, in order to clarify local inhomogeneities in ODS_WQ_RT, a TEM lamella was produced by FIB on a specific area (selected by SEM) with the above-mentioned Zeiss NVision 40 Cross-Beam.

Fracture surface characterization

The C(T) specimens were heat tinted after testing and then the halves were mechanically separated after cooling it in liquid nitrogen to permit visual access to the fracture surfaces. Stereoscopic microscopy and SEM SE imaging was performed on all primary fracture surfaces to understand the fracture mechanisms.

2.3 Tensile tests

Tensile tests were carried out by KIT on miniature cylindrical tensile specimens of ODS_AC_RT as sufficient material was not available for larger specimen testing. The specimen was 2 mm in diameter and 7.6 mm in nominal gauge length parallel to the rolling direction. The tests were performed in air with a crosshead speed of 0.1 mm/min in the temperature range from RT to 700 ˚C. The resulting initial strain rate was 2.38 x 10^{-4} s^{-1}. One specimen was tested at each temperature. The procedures and specimen design in the test were adherent to ASTM E8.

2.4 Quasi-static fracture toughness testing

Sub-sized compact tension C(T) specimen of 6.35 mm thickness (0.25T) were machined from ODS_WQ_RT and ODS_AC_RT in the L-T orientation. The cutting scheme of the specimen can be seen in Fig. 1. All the C(T) specimens were 20% side grooved and fatigue pre-cracked at RT with 14 MPa√m as the nominal cyclic stress intensity at the end of fatigue pre-cracking stage (K_{end}). A crack length to width ratio (a/W) of 0.5 was obtained using a resonance testing machine.

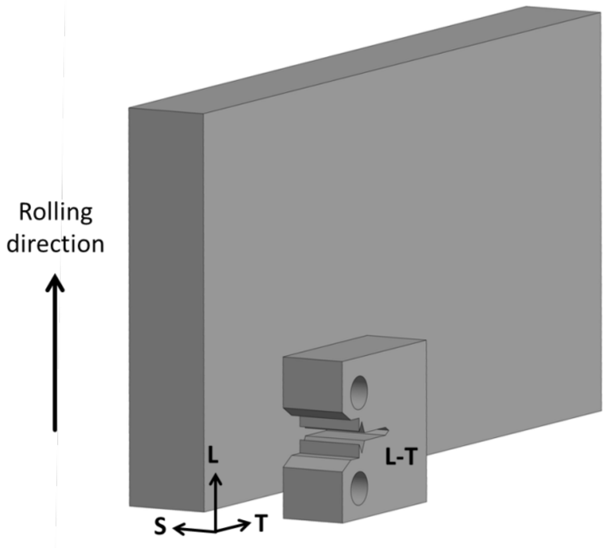

Fig. 1 Cutting scheme of the 0.25T C(T) specimens from ODS_WQ_RT and ODS_AC_RT in the L-T orientation

The unloading compliance method [28] was used to carry out quasi-static fracture toughness tests according to ASTM E1820-13 [29]. A 25% load drop and a 30 s relaxation time were associated with each unloading. Single tests were performed in air at temperatures of -100, 22, 100, 200, 300, 400 and 600 ˚C for ODS_WQ_RT. For ODS_AC_RT, the same testing temperatures, except 300 ˚C, were used. Unloading steps between 0.005 mm and 0.015 mm were used with a crosshead speed of 0.1 mm per minute. After approximately 2 mm crack propagation, the tests were stopped and specimens were heat tinted to identify the crack growth region. The tests performed at or above 400 ˚C required no additional heat tinting due to the oxidation at high test temperatures. Optical microscopy was used to measure the initial and the final primary crack lengths at the fracture surfaces according to the nine point standard ASTM E1820-13 method. The crack opening displacement (COD) measurements were performed at the front face. Therefore, the compliance and the displacement values were converted to the load line values [30]. Finally, the fracture toughness evaluation was performed according to ASTM E1820-13.

2.5 Nanoindentation

The inhomogeneous microstructure in ODS_WQ_RT was analysed using site-specific nanoindentation in order to investigate the different regions. A universal nanomechanical tester (Zwick GmbH) equipped with a Berkovich indenter was used to perform nanoindentation testing. A maximum indentation load of 50 mN was applied. The measurement cycle consisted of loading for 248 s following a quadratic function with a dwell time of 3 s, a creep segment at 50 mN for 20 s with a dwell time of 3 s, an unloading segment for 8 s where the load was reduced to 5 mN following a quadratic function, a holding segment for 60 s and a final unloading segment for 1.6 s. Two reference materials (fused silica, sapphire) with known elastic moduli were used for the calibration of the indenter area function and the instrument stiffness. Hertzian contact was assumed for the first several 10 nm of the loading curve for the zero point correction.

The short duration of the measuring cycle meant that a thermal drift correction was not necessary. Additionally, the system was allowed to equilibrate for at least 45 min prior to the measurements and was equipped with thermal insulation. Data analysis was performed using a method developed by Doerner and Nix [31], adapted to pyramidal indenters by Oliver and Pharr [32,33].

3 Results

3.1 Microstructure characterization

3.1.1 Optical microscopy

ODS_WQ_450 looks homogeneous under optical microscope with many sub-micron particles (size: 100 nm – 1000 nm) (Fig. 2a). Bright stripes parallel to the rolling direction were observed in ODS_WQ_RT (Fig. 2b) which were claimed as insufficient mechanically alloyed regions devoid of nano-particles [34]. The rest of the etched microstructure appeared homogeneous with many large sub-micron particles. It was reported previously that the microstructure of ODS_AC_RT too contained inhomogeneous regions appearing as “bright stripes” parallel to the rolling direction in bright-field optical microscopy images (Fig. 2c) [35]. It was found that these regions were insufficiently mechanically alloyed and were devoid of oxide nano-particles.

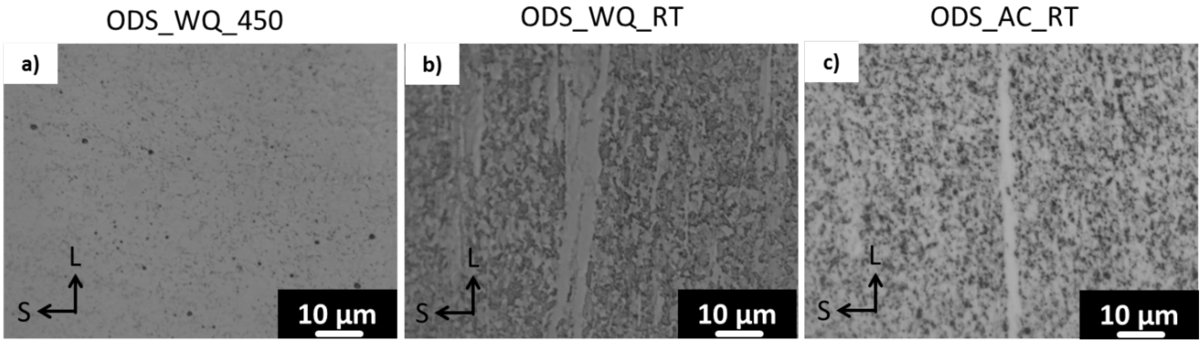

Fig. 2 Optical microscope images of the etched bulk microstructure of a) ODS_WQ_450, b) ODS_WQ_RT and c) ODS_AC_RT

3.1.2 SEM

SEM SE images of the etched specimen highlight the "larger" sub-micron particles which appear as bright dots primarily along grain boundaries in all the three alloys (Fig. 3). These sub-micron particles are pre-dominantly Cr, W and C rich precipitates of the $M_{23}C_6$ type as identified by STEM-EDX and SAD (shown later in Fig. 9 and Fig. 11, respectively).

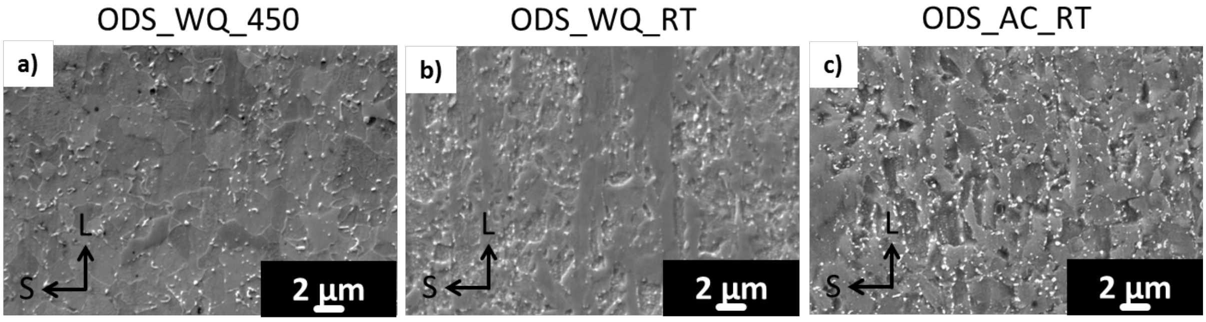

Fig. 3 SEM SE micrographs in the etched LS plane highlighting the sub-micron particles of a) ODS_WQ_450, b) ODS_WQ_RT and c) ODS_AC_RT

3.1.3 EBSD

The grain boundary maps of all the ODS steels obtained from EBSD measurements are presented in Fig. 4 for the LS plane. ODS_AC_RT and ODS_WQ_RT exhibit bimodal grain structure with more than 80 % of the grains in the ultra-fine grain (UFG) regime (below 1 µm in size) together with coarse grains; these ultra-fine grains exhibit an average size of 0.45 µm and 0.47 µm, respectively, in the two materials. Grains above a micron are classified as coarse grains. The coarse grains exhibit an average size of 1.56 µm and 1.63 µm for ODS_AC_RT and ODS_WQ_RT, respectively. The grain aspect ratios of both the materials are similar and not too high, as shown in Table 3 with the presence of elongated zones containing coarser grains arranged parallel to the longitudinal direction. In ODS_WQ_450, the ultra-fine and the coarse grains are more evenly distributed with sizes of 0.59 µm and 1.87 µm, respectively. The grains are more or less equiaxed with no specific arrangement in any particular direction. A detailed statistical grain size analysis of the ultra-fine and coarse grains in terms of equivalent circular diameter (the diameter of a circle with the same area as the grains), corresponding grain aspect ratio (GAR), number and area fraction are presented for all the materials in Table 3.

Typically, in ODS_WQ_450, there was no internal misorientation within the grains (Fig. 5a). Those grains that appeared to have some internal misorientation were mostly due to artefacts caused by the LAGBs between some of the grains. ODS_WQ_RT and ODS_AC_RT both exhibited a high internal misorientation within the grains (Fig. 5b and c).

Table 3 Grain size analysis for ultra-fine and coarse grains for the three ODS steels in the LS plane

Material	Ultra-fine grains (*d* ≤ 1 µm)				Coarse grains (*d* > 1 µm)				Average grain size (µm)
	Average size (µm)	Number fraction (%)	Area fraction (%)	GAR	Average size (µm)	Number fraction (%)	Area fraction (%)	GAR	
ODS_WQ_450	0.59	48.9	8.3	2	1.87	51.1	91.6	1.8	1.24
ODS_WQ_RT	0.47	81.6	27.1	2.2	1.63	18.4	72.9	2.4	0.68
ODS_AC_RT	0.45	85.5	33.4	2	1.56	14.5	66.6	2	0.61

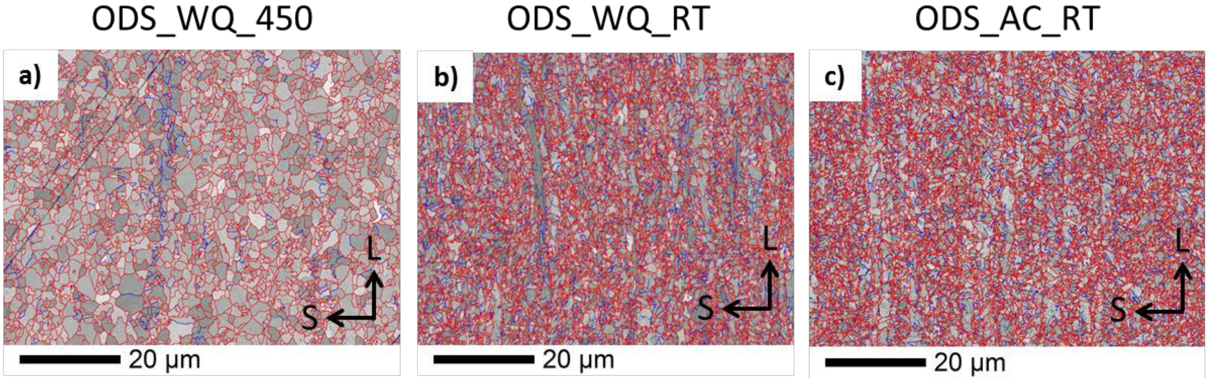

Fig. 4 EBSD grain boundary maps of a) ODS_WQ_450, b) ODS_WQ_RT and c) ODS_AC_RT specimens. HAGBs (grain boundary misorientation angle ≥ 15°) and LAGBs (grain boundary misorientation angle between 5° and 15°) are coloured red and blue, respectively.

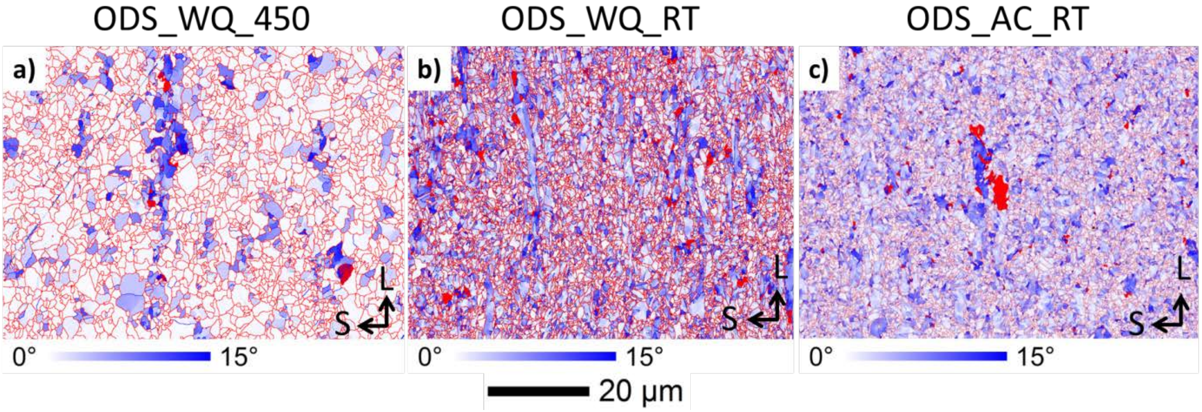

Fig. 5 Internal misorientation of a measured pixel with respect to the corresponding average grain orientation of a) ODS_WQ_450 b) ODS_WQ_RT and c) ODS_AC_RT. White colour indicates zero misorientation, transitioning towards blue with increasing misorientation. Red coloured points exceed 15° internal misorientation.

3.1.4 TEM

Eiselt et al. reported Y and Ti enriched nano-particles with their size ranging from 6 nm to 40 nm with a peak at 12 nm for ODS_WQ_450 [24]. For ODS_AC_RT, small angle neutron scattering (SANS) and TEM characterization of the nano-particles was performed [36]. The nano-particles had an approximately spherical shape and were enriched in Y and O, with a

Y:O ratio of 2:3 with minor amounts of Fe, Cr and Si. The average diameter of the nano-particles was 3.8 nm with a number density of 11.5 x 10^{22} m^{-3}.

In order to investigate the nano-particles in the bright stripe and the matrix region of ODS_WQ_RT using TEM, a FIB lift out was performed on ODS_WQ_RT to obtain a thin lamella that contained areas of both the bright stripe and the adjoined matrix (Fig. 6a). It was found that the bright stripe region contained finer nano-particles (size range: 1 - 4 nm) with a higher number density compared to the matrix which contained nano-particles in the size range 2 - 12 nm (Fig. 7). A similar TEM investigation has already been performed on ODS_AC_RT (Fig. 6d) where it was found that the bright stripes were devoid of oxide nano-particles (Fig. 6e) presumably due to insufficient MA, while an appreciably higher number of nano-particles were observed in the matrix (Fig. 6f) [35]. Their similar appearance under optical microscopy, as demonstrated in Fig. 2b and c, illustrates the necessity of an advanced study of these areas by means of TEM and nanoindentation in order to make a clear distinction.

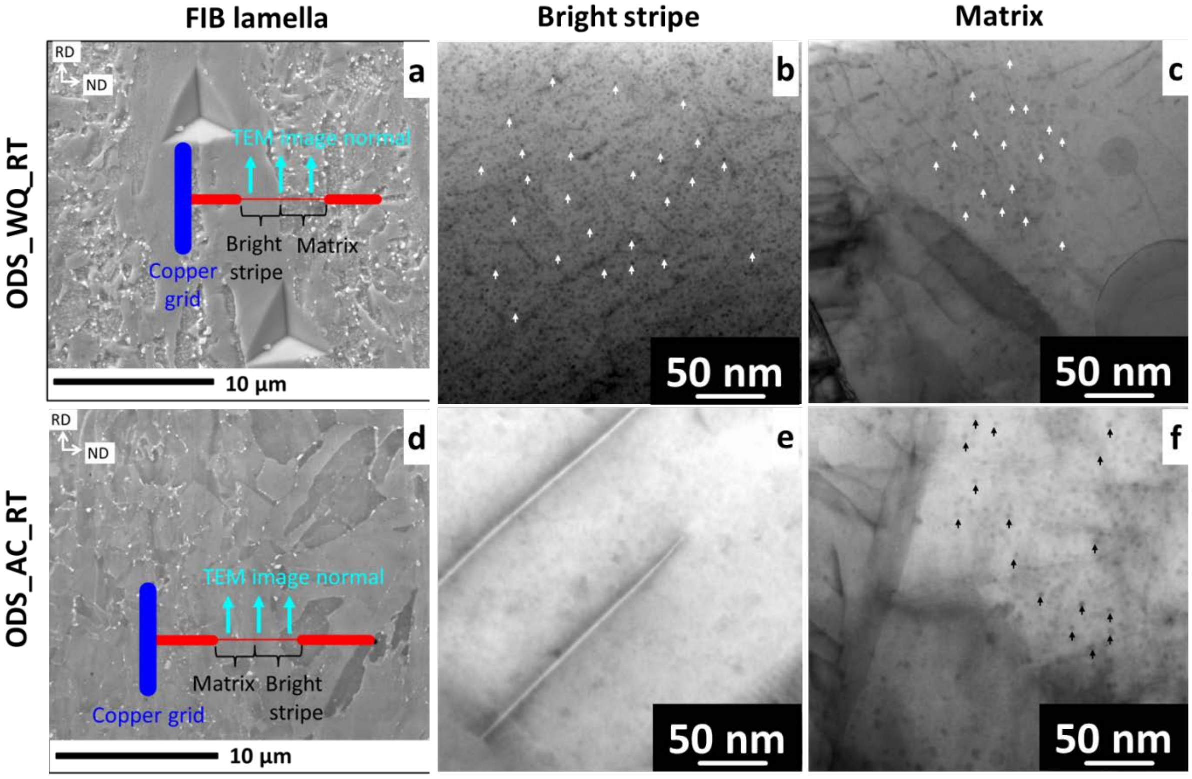

Fig. 6 SEM micrographs showing FIB lamella taken out from etched a) ODS_WQ_RT (nanoindents are visible) and d) ODS_AC_RT including areas from a bright stripe and the adjoining matrix region. (b and e) represent a STEM bright field image from the bright stripe region and (c and f) represent a STEM bright field image from the matrix region for ODS_WQ_RT and ODS_AC_RT, respectively. White and black arrows are used to indicate some of the nano-particles in ODS_WQ_RT and ODS_AC_RT, respectively. The two almost straight lines in e) are dislocations.

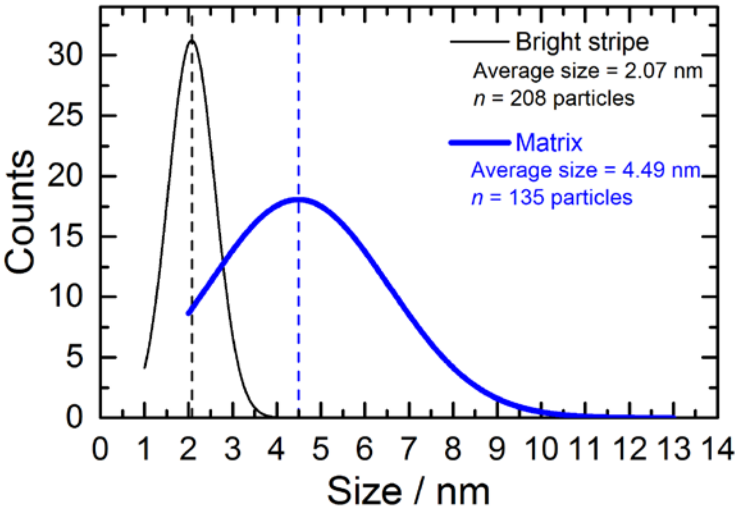

Fig. 7 Size distribution of the nano-particles in the bright stripe and matrix region of ODS_WQ_RT where *n* is the number of nano-particles examined.

With respect to the investigation of the sub-micron particles, the largest were found in ODS_WQ_450 followed by both ODS_WQ_RT and ODS_AC_RT in which these particles were similar in size (Fig. 8). In all the three materials, the bulk alloy predominantly consisted of many large Cr, W and C enriched sub-micron particles with a few smaller sub-micron particles enriched with Mn, V and O (Fig. 9). A detailed analysis of the size, number density, volume fraction along with the major and minor sub-micron particle enrichments for all the three materials can be found in Table 4. The longest and shortest size of the particles was measured in the sample area. The volume fraction of the sub-micron particles was obtained by assuming them as spheroids with half the longest dimension as the major axis and half the shortest dimension as the minor axis. In STEM-EDX, for the analysis of a particular sub-micron particle, the analysed volume contained not only the sub-micron particle, but additionally, a part of the matrix (many particles are smaller than the sample thickness, which was typically of order 200 nm). Therefore, the values given in Tables 4 and 5 indicate the general enrichment in the sub-micron particle composition and do not necessarily present the true composition.

The enriched sub-micron particle compositions (the largest examined) and the bulk compositions, found using STEM-EDX, are presented in Table 5 for all the materials. ODS_WQ_450 contained large sub-micron particles additionally enriched with O. The STEM-EDX spectra from the bulk and a sub-micron particle of ODS_WQ_450 presented in Fig. 10 distinguishes the C and O peaks at low energies. Similar C peaks were also observed for sub-micron particles in ODS_WQ_RT and ODS_AC_RT, but no O enrichment was found in them.

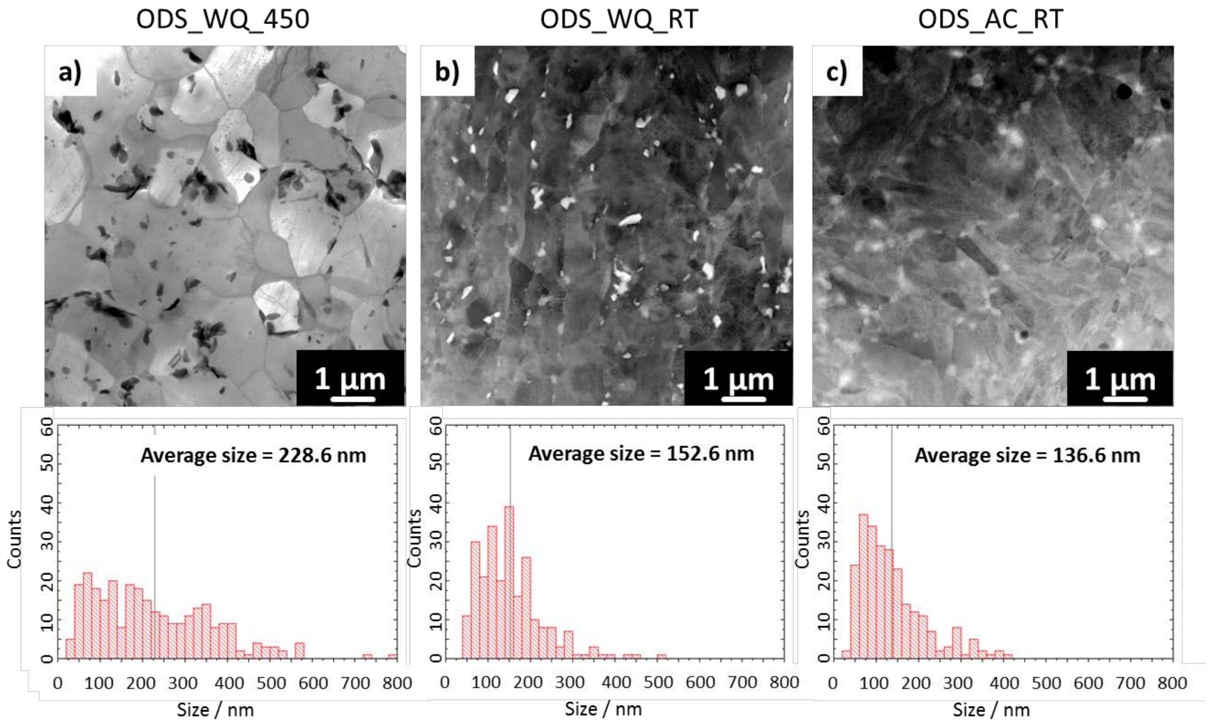

Fig. 8 Bright field STEM image of a) ODS_WQ_450 along with HAADF-STEM images of b) ODS_WQ_RT and c) ODS_AC_RT showing the sub-micron particles along with their size distributions.

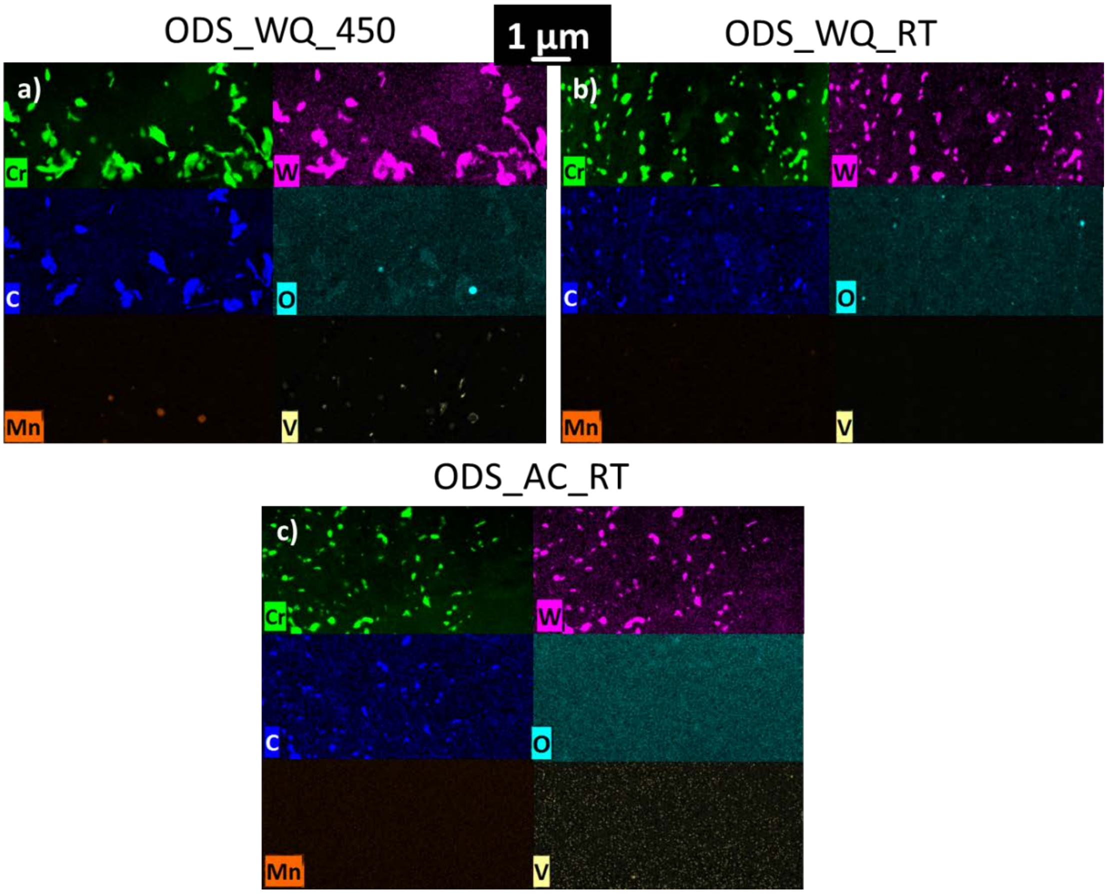

Fig. 9 STEM-EDX element mappings of a) ODS_WQ_450, b) ODS_WQ_RT and c) ODS_AC_RT showing sub-micron particles predominantly enriched with Cr, W and C (maps were not normalizedto enhance contrast between elements) with additional minor enrichments in O, Mn and V (shown in normalized maps).

Table 4 Sub-micron particles in all the three ODS steels found using STEM-EDX. The Cr maps of all the materials are used for obtaining the statistics on the larger particles.

Material	Particle enrichment		Average longest size (µm)	Average shortest size (µm)	Number density ($10^{19}/m^3$)	Volume Fraction
	Major	Minor				
ODS_WQ_450	**all**		**0.3**	**0.13**	**0.67**	**0.0175**
	C, W	Cr, O	0.31			
	C, O	Cr, W	0.29			
	O, Mn	V, Cr	0.22			
	V	O	0.13			
ODS_WQ_RT	**all**		**0.15**	**0.09**	**1.26**	**0.0084**
	Cr, W	-	0.16			
	C	W, Cr	0.15			
	O	Mn	0.07			
ODS_AC_RT	**all**		**0.14**	**0.08**	**1.32**	**0.0062**
	Cr, W	-	0.17			
	C	W, Cr	0.15			
	V	Cr	0.11			

Table 5 A comparison of the bulk composition and the enriched sub-micron particle compositions. The term enrichment is used here, since the analysed volume may contain the matrix along with the sub-micron particle. The bold values indicate the particle enrichments.

Element (wt. %)	ODS_WQ_450			ODS_WQ_RT			ODS_AC_RT		
	Bulk	C, W, Cr, O	C, O, Cr, W	Bulk	Cr, W	C, W, Cr	Bulk	Cr, W	C, W, Cr
C	0.45	**2.3**	**3.3**	0.4	0.1	**2.9**	0.3	0.2	**2.8**
O	0.38	**1.0**	**2.1**	0.3	0.7	0.5	0.6	0.6	0.6
V	0.21	0.3	0.2	0.2	0.3	0.2	0.2	0.4	0.3
Cr	7.94	**23.9**	**18.7**	7.1	**29.6**	**19.3**	6.7	**34.1**	**20.3**
Mn	0.69	0.9	0.8	0.6	1.0	0.8	0.6	1.1	0.9
Fe	89.3	68.1	72.6	90.4	64.1	73.3	90.6	58.8	72.1
W	1.07	**3.5**	**2.3**	1.0	**4.1**	**2.9**	1.0	**4.8**	**3**

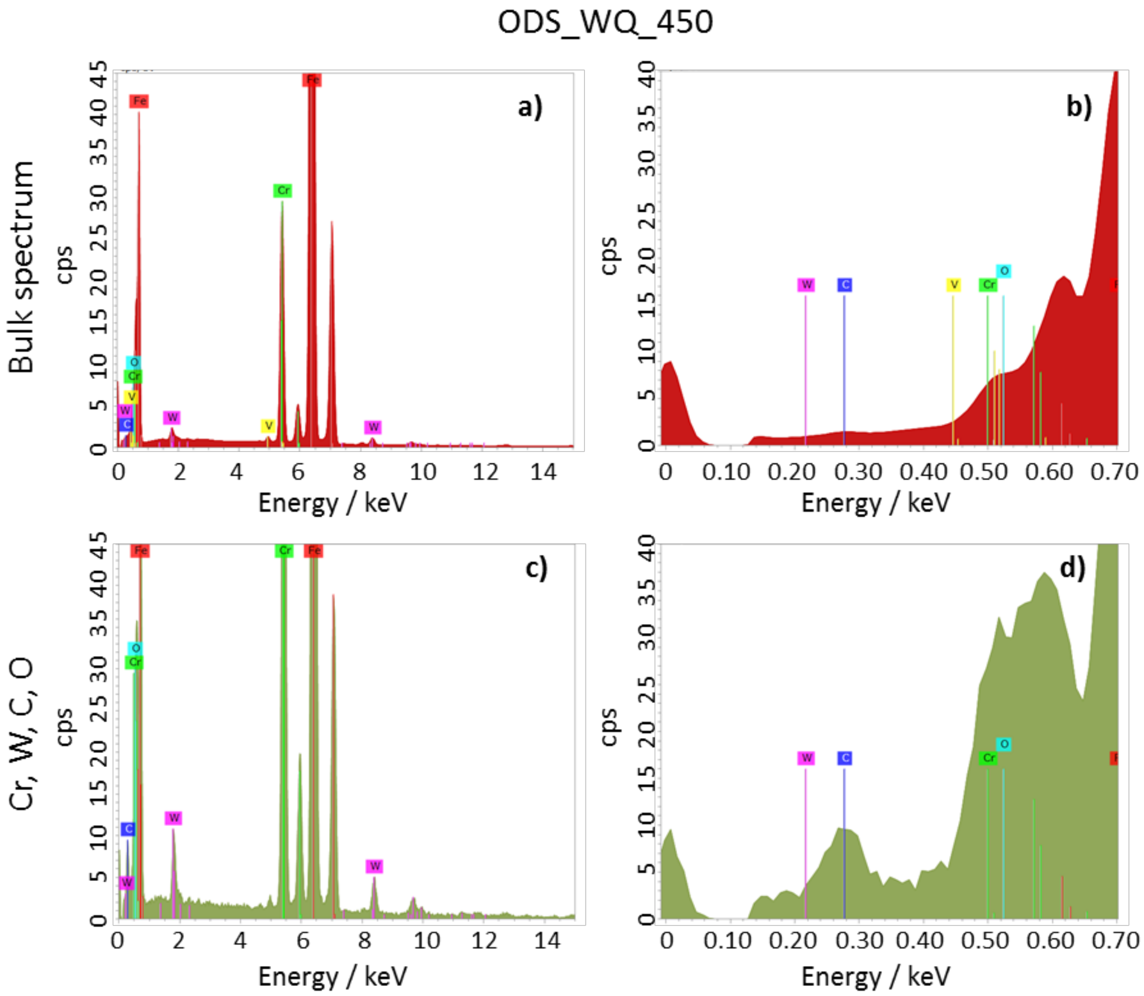

Fig. 10 STEM-EDX spectra represented by counts per second (cps) versus energy plots from a) the bulk and c) a C, O, Cr, W enriched sub-micron particle of ODS_WQ_450. b) and d) shows the spectrum at low energy values to distinguish the C and O peaks in the bulk and the sub-micron particle, respectively

Fig. 11 presents a SAD pattern obtained for ODS_AC_RT. Apart from diffraction rings that correspond to the iron grains, several diffraction spots were observed. To obtain the lattice constant from all spots, the evaluation was done relative to the iron spots in order to gain the best possible accuracy. Assuming the presence of $M_{23}C_6$ carbides with a face cubic centred (fcc) structure and a lattice constant of 1.06 nm and an iron lattice constant of 0.286 nm, many of these spots can be indexed, as demonstrated by green circles in Fig. 11. However, there are additional spots that are not in agreement with this assumption; several examples are marked by red circles in Fig. 11. Most of these additional spots cannot be explained by possible diffraction from larger Y_2O_3 particles, assuming a bcc lattice and a lattice constant of 1.065 nm for Y_2O_3. Consequently, there are likely different types of particles inside the diffraction volume, which is in agreement with the EDX analysis.

In the other two ODS alloys, diffraction patterns indicate similar result (patterns had inferior quality and hence are not presented here): diffraction spots from fcc $M_{23}C_6$ carbides and some unidentified additional particles were present. Applying SAD, the amount of diffraction spots from a chosen area is limited, and therefore, completeness cannot be guaranteed. While SAD provides evidence that all three ODS alloys contain $M_{23}C_6$ carbides, SAD is insufficient to determine whether the additional spots (and particles) are the same for all three

ODS steels. A careful X-ray diffraction analysis (not done here) may provide additional information; however, this characterization is beyond the scope of the present work.

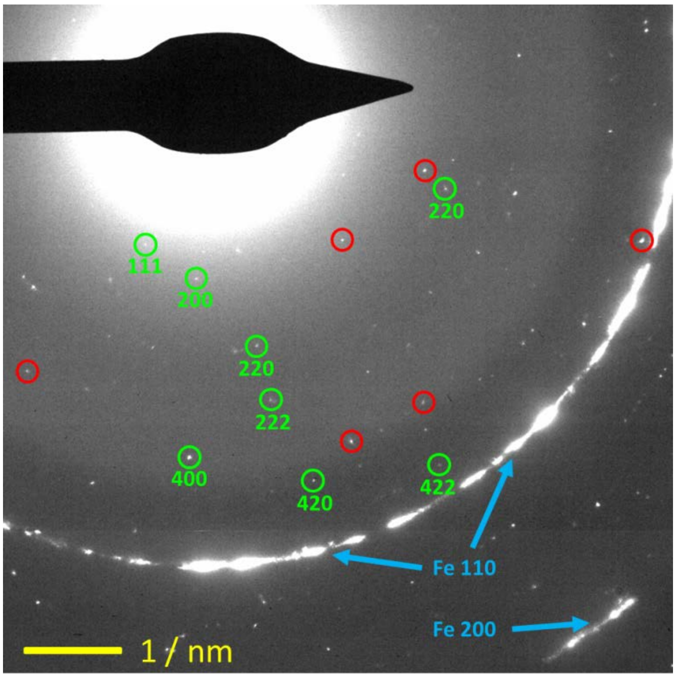

Fig. 11 Subset of a selected area diffraction (SAD) pattern recorded in ODS_AC_RT. The contrast is artificially increased to visualize the weaker diffraction spots. Blue arrows point to the 110 and 200 diffraction rings of the iron grains. Green circles correspond to reflections from $M_{23}C_6$ carbides, red circles indicate particles with lattice constants different from $M_{23}C_6$

3.2 Nanoindentation

Nanoindentation was performed on the bright stripes and matrix region of ODS_WQ_RT. Two series of indentations were performed on multiple bright stripes containing 7 and 13 indents, respectively while one series of 9 indents was performed on the matrix. An average load displacement curve was calculated from the single corrected curves of several indents, with a spacing of 30 µm in the matrix and with a spacing of 10 µm in the bright stripes, placed in such a manner to avoid interference by neighbouring indents. To calculate the average curve, the load or holding time in case of the holding segment, is divided into intervals and the data points of all curves within this interval are averaged. The standard deviation for load and displacement was calculated for each interval and was used to calculate the statistical errors in the subsequent analysis.

A plot of indentation hardness variation with the contact depth for ODS_WQ_RT can be found in Fig. 12a along with the a similar plot for ODS_AC_RT in Fig. 12b (data obtained from [35]). It is clear that the bright stripes in ODS_WQ_RT were slightly harder than the matrix, which was opposite of what was observed in ODS_AC_RT (Fig. 12b) [35]. A reference depth of 400 nm was chosen to eliminate the uncertainties associated with low load measurements [37] and not exceed the thickness of the bright stripe. In ODS_WQ_RT, the average indentation hardness values measured at the reference depth of 400 nm for the matrix was 4.14 ± 0.40 GPa while it was 4.48 ± 0.33 GPa for the bright stripes.

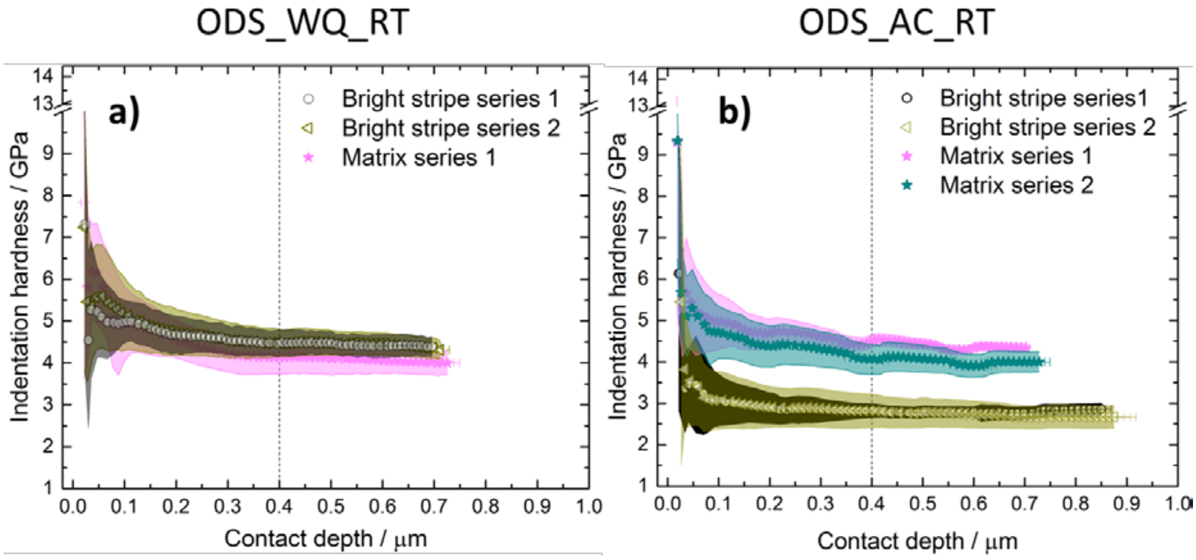

Fig. 12 Plots indicating indentation hardness as a function of contact depth for a) ODS_WQ_RT and b) ODS_AC_RT (data obtained from [35])

3.3 Tensile tests

Yield strength (σ_y) and total elongation (ε_t) are presented in Fig. 13 for ODS_AC_RT for temperatures ranging from RT to 700 ˚C and the tensile test data can be found in Table 6. Tensile data for ODS_WQ_RT from McClintock et al. [15] and Byun et al. [18] and for ODS_WQ_450 from Chaouadi et al.[23] are also plotted in the same figure for comparison. The tensile test conditions (strain rate, sample size etc.) were similar for all materials and the same can be stated about the observed trends. The yield strength values of the different alloys decreases gradually up to ≈ 400 ˚C. At temperatures above ~400°C, the yield strength drops at a steeper rate. ODS_WQ_RT exhibited the highest yield strength values at all temperatures. This is followed by ODS_AC_RT which exhibited higher yield strength than ODS_WQ_450 up to 400 ˚C. ODS_AC_RT and ODS_WQ_450 exhibited similar yield strength values above 400 ˚C.

The total elongation values remained relatively stable for all alloys up to 400 ˚C, above which it increased, reaching a maximum value above 600 ˚C. Up to 500 ˚C, the total elongation of ODS_WQ_450 was the highest followed by ODS_AC_RT and ODS_WQ_RT. Above 500 ˚C, ODS_AC_RT exhibited the highest total elongation values.

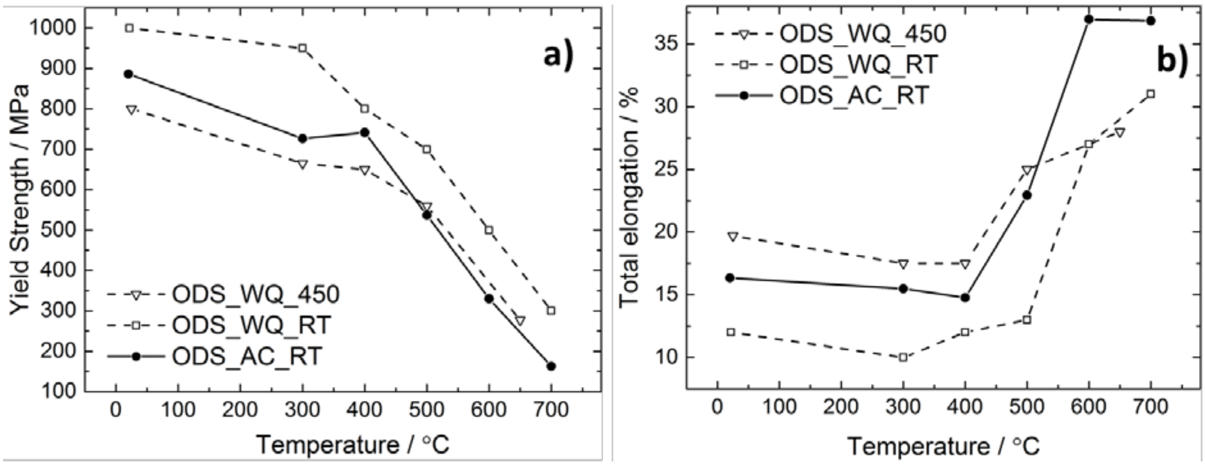

Fig. 13 a) Yield strength (σ_y) and b) total elongation (ε_t) as a function of temperature for ODS_AC_RT in the longitudinal direction. For ODS_WQ_RT, the tensile test data has been obtained from McClintock et al.[15] & Byun et al. [18] and for ODS_WQ_450, it has been obtained from Chaouadi et al.[23].

Table 6 Tensile test data for ODS_AC_RT

Temperature (˚C)	Yield Strength σ_y (MPa)	Ultimate tensile strength σ_{UTS} (MPa)	Uniform elongation ε_u (%)	Total elongation ε_t (%)
RT	886	1066	3.5	16.4
300	727	913	2.5	15.5
400	741	840	1.9	14.8
500	537	685	1.5	22.9
600	330	428	2.9	37
700	163	247	15.3	36.8

3.4 Fracture toughness tests

The fracture toughness for ODS_WQ_RT and ODS_AC_RT is plotted as a function of temperature in Fig. 14. Fracture toughness is represented by J_Q values which are provisional J_{IC} values determined by the intersection of the J-R curve with a 0.2 mm offset line. Additionally, the fracture toughness values are provided in Table 7; samples that exhibited unstable crack propagation are suffixed with “U”. Insufficient ODS_WQ_450 material was available to perform experiments similar to the other two ODS steels, therefore the fracture toughness values from Chaouadi et al.[23] in the temperature range of 300 ˚C to 650 ˚C were used for comparison. At -100 ˚C and RT, the fracture toughness of ODS_WQ_450 are taken from Lucon et al. [3,38]. A dotted line in Fig. 14 is used to connect the two set of values for ODS_WQ_450. Differences due to size effects and different experimental setups were not assumed to be significant as most of the tests were performed on similar reduced sized specimens (6 mm thickness). Only the tests at -100 ˚C and RT of ODS_WQ_450 (from Lucon et al. [3,38]) were performed with specimen sizes smaller than the rest of the test specimens (3 mm thickness). Hence these fracture toughness values are expected to be higher (grey symbols in Fig. 14).

At -100 ˚C, ODS_AC_RT experienced unstable fracture and exhibited low fracture toughness. At and above RT, the fracture toughness increased above J_Q = 45 kJ/m^2 (represented by a dashed line in Fig. 14) and reached its highest value at 100 ˚C. Byun et al. [18] considered J_Q = 45 kJ/m^2 ($K_{JQ} \geq 100$ MPa√m) an acceptable limit of fracture toughness for ODS steels for engineering applications. At 200 ˚C and 400 ˚C, the fracture toughness decreased and at 600 ˚C, the fracture toughness dropped back to low values.

ODS_WQ_RT exhibited higher fracture toughness than ODS_AC_RT at lower temperatures (-100 ˚C and RT) while above 100 ˚C, the fracture toughness values for the two alloys were similar (Fig. 14). ODS_WQ_450 in comparison exhibited the lowest fracture toughness at lower temperatures (-100 ˚C and RT). Even though the fracture toughness decreased above 300 ˚C, ODS_WQ_450 exhibited significantly higher fracture toughness at temperatures between 300 ˚C and 500 ˚C compared to the other two ODS steels. Above 500 ˚C, the fracture toughness of ODS_WQ_450 is only slightly higher than the other two ODS steels.

Table 7 Fracture toughness (J_Q) values for ODS_WQ_RT and ODS_AC_RT at various temperatures for the L-T orientation

Temperature °C	ODS_WQ_RT J_Q (kJ/m^2)	ODS_AC_RT J_Q (kJ/m^2)
-100	79.2	5.3U
22	120.2	59
100	103.6	102
200	118	96.8
300	107.9	-
400	47.1	60.8
600	5.9	12.8

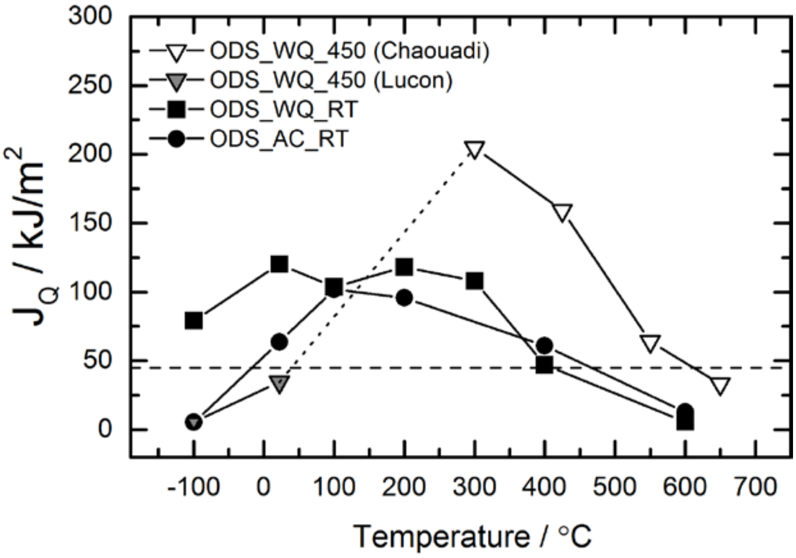

Fig. 14 Fracture toughness comparison over a wide temperature range for ODS_AC_RT and ODS_WQ_RT along with ODS_WQ_450 (taken from Chaouadi et al.[23]). For ODS_WQ_450, the results for -100 ˚C and 22 ˚C are taken from Lucon et al. [3,38] (grey symbols). A dotted line is used to connect the two set of values for ODS_WQ_450. The dashed line indicates the acceptable fracture toughness value of J_Q = 45 kJ/m^2 (K_{JQ} = 100 MPa√m) [18]

3.5 Fracture surfaces

From the macroscopic stereo microscope images it was clear that ODS_WQ_RT exhibited significant amount of secondary cracking from -100 ˚C to 100 ˚C (Fig. 15). The amount of secondary cracking reduced as the temperature increased. ODS_AC_RT on the other hand exhibited a featureless flat fracture surface at -100˚C, a fracture surface with partial secondary cracking at RT, and a fracture surface without secondary cracks at 100 ˚C. At and above 200 ˚C, both the materials exhibited no secondary cracking.

On a microscopic level, the primary crack growth region (heat tinted darker regions of Fig. 15) consisted of dimples from -100 ˚C to 400 ˚C for ODS_WQ_RT (Fig. 16). This was also true for ODS_AC_RT but for a temperature range of RT to 400 ˚C. At -100 ˚C, ODS_AC_RT exhibited a flat fracture surface with multiple facets. At 600 ˚C, both the materials exhibited particle like features on the fracture surface devoid of any dimples.

For ODS_WQ_450, dimples were observed by Chaouadi et al. [23] for fracture surfaces tested between 300 ˚C and 550 ˚C while particle like features were observed for the fracture surface tested at 650 ˚C.

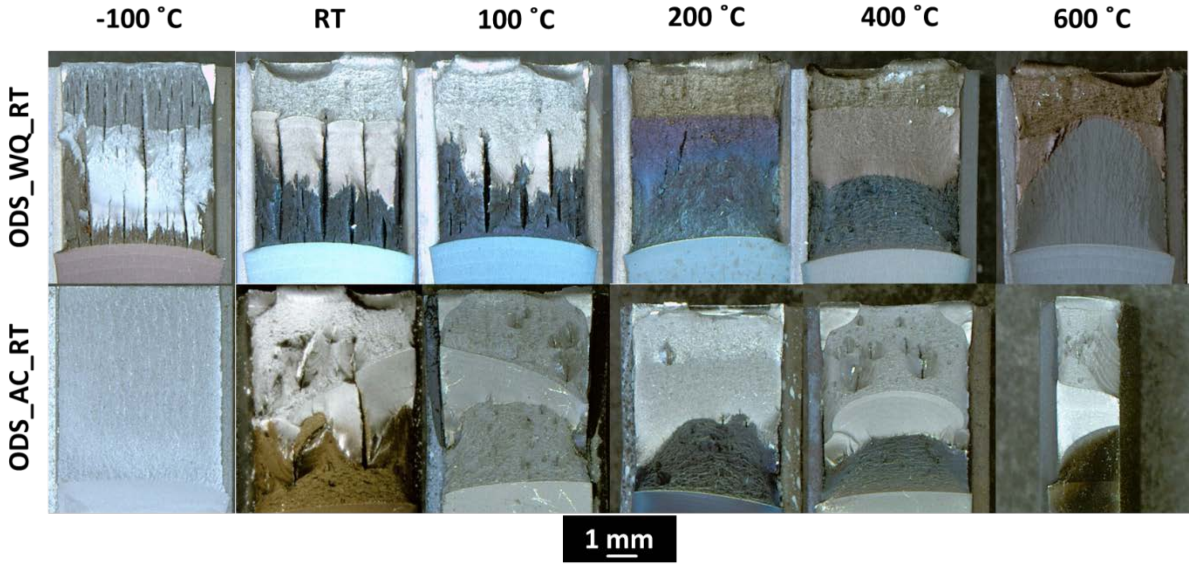

Fig. 15 Stereo microscope macroscopic images of fracture surfaces of ODS_WQ_RT and ODS_AC_RT at different temperatures

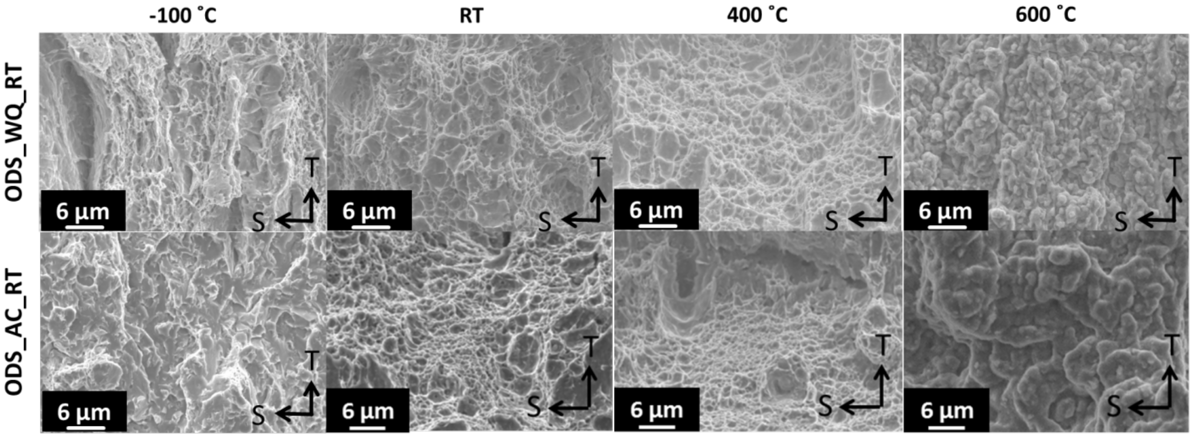

Fig. 16 SEM SE images of fracture surfaces of ODS_WQ_RT and ODS_AC_RT at different temperatures

4 Discussion

4.1 Microstructure characterization

ODS_WQ_450 was austenitized at 1100 ˚C and then water quenched to 450 ˚C, which is above the martensite start temperature ($M_S \approx 350$ ˚C [11]). Further tempering and cooling leads to ferrite formation. Hence its microstructure consists only of globular ferrite grains and no martensitic packets, sub-grains or laths were observed (Fig. 8a). The internal misorientation in the grains was very low (Fig. 5a) which confirms a ferrite phase formed by phase transformation via iron diffusion.

Klimiankou et al. reported martensitic grains, characterized by a lath structure and a high dislocation density for ODS_WQ_RT [9]. The lath structure was corroborated by the TEM image (Fig. 8b) while the internal misorientation map (Fig. 5b) confirmed the presence of multiple LAGBs formed due to dislocations introduced via the martensitic transformation. For ODS_AC_RT, it was reported that the air cooling rate was high enough to form martensite [35] which was corroborated by both the TEM image and the internal misorientation map (Fig. 8c and Fig. 5c). In the following, a possible sequence of the microstructure evolution during the manufacturing of these two materials is suggested:

1. Shortly before and during the hot-rolling process at 1150 ˚C, austenitization already begins, due to the high driving pressure in ferrite. Due to the large deformation and high temperature, dynamic recrystallization sets in at certain parts of the plate, resulting in a bimodal microstructure.
2. Afterwards, a separate heat treatment at 1100 ˚C for 30 minutes completes the austenitization process. As carbides begin to dissolve, equiaxed austenite grains start to form at the carbide-ferrite matrix interfaces [7]. Due to the pinning effect by the nano-particles in the microstructure, the prior austenite grains (PAGs) are fine sized (of the order of a few µm). A similar fine-grained microstructure was reported in [11].
3. Subsequent water/air cooling to RT leads to the formation of martensite inside the PAGs. Precipitation of carbides rich in Cr, W and Fe takes place at the PAG boundaries and the lath boundaries. Similar results were also reported in [10].
4. Tempering at 750 ˚C for 2 hours leads to diffusion and recovery resulting in the partial transformation of martensite lath boundaries to sub-grain boundaries along with formation and coarsening of the $M_{23}C_6$ carbide precipitates at grain boundaries. The SEM SE image of the etched bulk material in Fig. 3 also shows these coarsened carbides at grain boundaries. A similar microstructure was reported in previous publications [9,10].

The tempered martensite grains formed from PAGs are bimodal in nature with a continuous harmonic structure, which consists of coarse grained islands in a matrix of ultra-fine grains. Such microstructures were reported for several pure metals and alloys [39–42] and were found to provide a good balance of a high yield strength and high ductility, both of which are beneficial for fracture toughness.

A non-intuitive microstructural difference between ODS_WQ_RT and ODS_AC_RT is that although the elongated inhomogeneous regions or the “bright stripes” in both these materials look identical under optical microscopy (Fig. 2b and c), they are not the same. Residual α-ferrite forms during the incomplete reverse transformation of α-ferrite to γ-austenite during the austenitization step at 1100 ˚C due to the blocking of α-ferrite/γ-austenite interfaces by nano-particles in the matrix [6,19,20,43–49]. This phase is reported to be responsible for providing superior creep and high-temperature strength to ferritic-martensitic ODS steels [6,44,50–52]. Residual ferrite was reported to be harder and contains finer and higher number density of oxide nano-particles than the matrix [6,7]. Indeed, the results indicate that the bright stripes in ODS_WQ_RT are residual α-ferrite phases as they are harder than the matrix (Fig. 12a) and contain finer and higher number density of oxide nano-particles than the matrix (Fig. 6a-c and Fig. 7). The residual ferrite phase cannot fully be expected to be free of internal misorientation as in the case of recrystallized ferrite grains, due to strains introduced by neighbouring grains which underwent the martensitic transformation and therefore may contain LAGBs. Indeed, a noteworthy internal misorientation was observed in these bright stripes (Fig. 5b).

On the other hand, it was reported by Das et al. that the bright stripes in ODS_AC_RT were were softer than the matrix (Fig. 12b) and were devoid of oxide nano-particles (Fig. 6e) [35]. Due to the lack of oxide nano-particles, the α-γ transformation was not blocked during austenitization and thus residual ferrite can be ruled out in the bright stripes. The likely explanation for the formation of these bright stripes is imperfect mechanical alloying which results in the absence of nano-particles in the bright stripes. This leads to higher grain boundary mobility, larger grain size and lower number of grain boundary carbides which results in the distinct etching behaviour of these regions [35].

4.2 Microstructure – fracture toughness correlation

General considerations

Some of the fracture toughness tests conducted at lower temperatures (especially at -100 ˚C of ODS_AC_RT) resulted in transgranular cleavage fracture which typically produces a multi-faceted flat fracture surface (Fig. 15 and Fig. 16). Brittle cleavage fracture is dependent on material parameters such as sub-micron particle size, volume fraction, matrix ductility and grain boundary strength. It is especially sensitive to the size and distribution of carbides in the microstructure [53,54].

At higher temperatures (100 ˚C ≤ T ≤ 500 ˚C), the fracture surfaces predominantly exhibit dimples indicative of transgranular ductile fracture (Fig. 16). The fracture toughness in the ductile regime also depends on the factors mentioned above but is predominantly sensitive to the matrix ductility or the strain hardening ability of the material.

At T > 500 ˚C, the fracture surface morphology changes from dimples to particle like features indicative of grain boundary decohesion (Fig. 16). Similar features on the fracture surface were also observed for other ODS steels [12,55–59]. Due to these observations, it is thought that at elevated temperatures the fracture toughness of these ferritic martensitic ODS alloys is predominantly controlled by the grain boundary strength.

Fracture toughness of a material, in general, is dependent on the following parameters over a wide range of temperatures:

4.2.1 Sub-micron particle size

At low temperatures, large sub-micron particles can fracture and initiate crack propagation causing brittle fracture [60]. At higher temperatures, ductile fracture occurs, where a void can be nucleated by sub-micron particle cracking or by its decohesion with the matrix. The interfacial strength between sub-micron particles and the matrix depends on the local chemical composition. Most studies indicate that void nucleation occurs at the larger sub-micron particles [61,62], which therefore control the fracture toughness of a material. Particles below 100 nm typically do not contribute to void nucleation directly but can contribute indirectly [62]. The nano-particles block dislocation motion which results in an increase of the yield strength. An increase in the yield strength is usually associated with a decrease in ductility and fracture toughness.

4.2.2 Sub-micron particle volume fraction

The fracture toughness of a material decreases with an increase in the volume fraction of sub-micron particles. This was reported experimentally by Lee et al. [63] for brittle fracture in reactor pressure vessel steels and by Edelson and Baldwin for ductile fracture in two phase alloys [64]. Additionally, Srivastava et al. [65] and Gao et al. [66] using simulations of ductile fracture reported the same trend.

4.2.3 Secondary cracking

Secondary cracks propagate in a plane perpendicular to the primary crack plane and are formed due to constraint-induced stress. Constraint induced stress acts in a direction perpendicular to the primary stress and exists in thick samples where, due to high stresses close to the crack front, the material nearby the crack front tries to contract but is resisted by the bulk material surrounding it (plain strain in the centre of the sample). Secondary cracking has been observed in various hot-rolled ODS steels due to microstructural anisotropy [55,57,67–72] and, experimental data and 3D finite element analysis has shown that they can increase energy absorption hence increasing the fracture toughness [55,73,74].

4.2.4 Matrix ductility

Fracture toughness is dependent on the ductility or the strain hardening ability of the material [75], which, in general for ductile materials, tends to decrease with increasing yield strength [76]. The yield strength of a material can be influenced by a number of factors, predominantly including the nano-particle type, size, and number density; dislocation density; and grain size.

4.2.5 Grain boundary strength

In the brittle regime, grain boundary strength can reduce due to segregation of impurities at the grain boundaries while in the ductile regime; it does not play a major role in controlling the fracture toughness. At relatively high temperatures (T > 500 ˚C), grain boundary strength controls the fracture toughness. Grain matrix deformation and grain boundary sliding were reported as the dominant deformation mechanisms [58] which occur due to weakened grain boundaries [59]. Some works suggest a higher dislocation activity at weakened grain boundaries as the primary cause for grain boundary strength reduction [12,58,77] while others attribute it to the segregation of solute atoms at the grain boundaries [57,78]. This leads to cavities at the grain boundary [79] and a shallow plastic zone [55] that lowers the fracture toughness. Materials with finer grains exhibit higher grain boundary area per unit volume, and hence are more prone to intergranular fracture at high temperatures.

4.3 Comparison of the ODS EUROFER steels

4.3.1 ODS EUROFER vs non-ODS EUROFER

Using sub-size KLST (kleinstprobe) specimens, Lindau et al. reported that non-ODS EUROFER exhibited higher upper shelf energy and a lower ductile to brittle transition temperature (DBTT) as compared to different batches of ODS EUROFER [1]. Master curve testing at a lower temperature range (below RT) [3] and fracture toughness testing at higher temperatures (300 ˚C to 650 ˚C) [23] also confirm higher fracture toughness for non-ODS EUROFER steels. This can be attributed to the higher ductility of non-ODS EUROFER steels as compared to ODS EUROFER steels [3]. The higher ductility in non-ODS EUROFER is a direct consequence of lower yield strength. Additionally, ductility is enhanced by the coarse grain structure in non-ODS EUROFER in which an average PAG size close to 15 µm was reported by Zilnyk et al. [11]. In comparison, the reported PAG size in ODS EUROFER is almost an order of magnitude smaller due to pinning of PAG boundaries by nano-particles. Furthermore, it was reported that the amount of retained austenite was higher in non-ODS EUROFER in comparison to ODS EUROFER which also contributes towards its ductility [11].

4.3.2 ODS_WQ_RT vs ODS_AC_RT

At temperatures close to the ductile to brittle transition regime of the two materials (-100 ˚C and RT), where brittle fracture plays a major role, ODS_WQ_RT exhibits higher fracture toughness and more stable fracture behaviour as compared to ODS_AC_RT (Fig. 14). This is not intuitive as the volume fraction and sizes of sub-micron particles, which are critical parameters for crack initiation in brittle fracture, in both these materials are similar (bold values in Table 4). The primary reason for the higher toughness observed in ODS_WQ_RT is the occurrence of higher amount of secondary cracking (Fig. 15), which is a by-product of the delamination phenomenon in the crack-divider geometry [80]. Secondary cracking occurs due to microstructural anisotropy however, in this work, most of the microstructural anisotropy is eliminated, due to the phase transformation of the 9Cr ODS EUROFER steels. Only elongated inhomogeneous regions (bright stripes) are left in both of the materials. In this case, the extensive secondary cracking in ODS_WQ_RT may be explained by the mismatch of mechanical properties between the elongated hard residual ferrite phases (Fig. 12a) containing finer nano-particles (Fig. 7) and the soft tempered martensite matrix. The constraint-induced stress deforms the softer matrix more than the harder residual ferrite phases resulting in secondary cracks at the interface of these two regions. It was also reported that secondary cracks were beneficial for preventing cleavage fracture [2,74] and for the stabilization of primary cracks [72]. Indeed, this was observed in the present work where secondary cracks in ODS_WQ_RT at low temperatures prevented unstable fracture and supported the formation of a ductile primary crack growth region (heat tinted region in Fig. 15). On the contrary, ODS_AC_RT exhibits no secondary cracking at -100 ˚C resulting in unstable brittle fracture and exhibits partial secondary cracking at RT resulting in stable fracture but lower fracture toughness. The inhomogeneous regions in ODS_AC_RT are softer than the matrix (Fig. 12b) and hence both the regions deform similarly with the constraint induced stress which may explain why ODS_AC_RT is less prone to secondary cracking as compared to ODS_WQ_RT.

At temperatures between 100 ˚C and 500 ˚C, both the materials exhibit more or less similar fracture toughness (Fig. 14). Here, the fracture toughness is primarily controlled by the matrix ductility of the material. The similar value of total elongation of the two materials in this temperature range confirms this (Fig. 13b). With the data presented in Fig. 14, a discussion of minor differences between ODS_WQ_RT and ODS_AC_RT with respect to the measured fracture toughness values above 100 °C is not meaningful, assuming that the statistic experimental error of J_Q is typically of the order 10 kJ/m^2 and measurements were not repeated. The lack of significant differences is understandable, as both alloys have very similar microstructural parameters that are important for fracture toughness; microscopic analysis showed the grain size, grain shape, volume fraction and size distribution of the sub-micron particles as well as their composition are similar for both alloys (with the exception of the bright stripe regions).

At temperatures above 500 ˚C, the total elongation of ODS_AC_RT becomes higher than ODS_WQ_RT (Fig. 13b). However, this is not reflected in the fracture toughness curves which indicate similar reduced fracture toughness values for the two materials (Fig. 14). This can be explained by a shift in fracture mechanism at this temperature range from transgranular ductile to intergranular fracture. At these elevated temperatures matrix ductility no longer predominately controls the fracture toughness and grain boundary weakening plays an important role leading to intergranular fracture as shown in Fig. 16 at 600 ˚C.

4.3.3 ODS_WQ_450 (ferritic) vs others (martensitic)

At lower temperatures (-100 ˚C and RT), ODS_WQ_450 exhibits the lowest fracture toughness (Fig. 14). This is likely because it contained the largest sub-micron particles (Fig. 8 and Table 4). There could also be a detrimental effect of larger sub-micron particles enriched with C and O on the brittle fracture behaviour of ODS_WQ_450 (Table 5); similar oxide particles were also reported in [8]. No information about the occurrence of secondary cracks on the fracture surfaces could be obtained from [23].

At higher temperatures (300 ˚C ≤ T ≤ 500 ˚C), ODS_WQ_450 exhibits the highest fracture toughness which can be explained by its higher matrix ductility (confirmed by the total elongation in Fig. 13b). This can qualitatively be attributed to its coarser ferritic grains with higher strain hardening ability and a lower dislocation density relative to the lower matrix ductility exhibited by the hard martensitic matrix of the other two materials.

At temperatures above 500 ˚C, the total elongation of ODS_WQ_450 is lower than ODS_AC_RT. However, this is not reflected in the fracture toughness curves which still show higher fracture toughness values of ODS_WQ_450 (Fig. 14). This can again be explained by a change in fracture mechanism from transgranular ductile to intergranular fracture. The coarse grained ODS_WQ_450 performed better at higher temperatures in terms of fracture toughness as it contained lower grain boundary area per volume of material.

5 Conclusions

- Three batches of 9Cr ODS EUROFER with varying thermo-mechanical processing history were investigated with respect to the effect of changes in microstructure on the fracture toughness.
- At lower temperatures (-100 ˚C and RT), ODS_WQ_RT exhibited the highest fracture toughness due to secondary cracking induced by hard residual ferrite phases. The least fracture toughness was exhibited by ODS_WQ_450 due to the presence of large sub-micron particles enriched with O.
- At higher temperatures (100 ˚C ≤ T ≤ 500 ˚C), ODS_WQ_450 exhibited the highest fracture toughness due to a ductile ferrite matrix, while both the martensitic ODS steels exhibited similar lower fracture toughness due to lack of matrix ductility.
- At T > 500 ˚C, weakening of grain boundary strength predominantly controls the fracture toughness resulting in higher fracture toughness for the ferritic steel ODS_WQ_450 due to its coarse-grained microstructure and results in lower fracture toughness values for both finer-grained martensitic steels.
- These results demonstrate that the thermo-mechanical processing route is an extremely important consideration for ferritic martensitic ODS steels, asvariations in heat treatment lead to significant differences in microstructure and fracture toughness.

Acknowledgements

The authors would like to thank Dr. Rachid Chaouadi from SCK-CEN, Belgium for providing ODS material for microstructural characterization.

We thank Mr. Wolfgang Webersinke and Mr. Mario Houska for their contributions to the fracture mechanics testing of C(T) specimens, Ms. Michaela Rossner for metallographic preparations and Ms. Annette Kunz for FIB sample preparation. Additional thanks goes to our colleagues Ulrich Skorupa and Jens Pietzsch at the workshop.

Support by the Structural Characterization Facilities at the HZDR Ion Beam Center (IBC) is gratefully acknowledged. The chemical analysis of the bulk ODS_AC_RT was performed by Dr. Thomas Bergfeld, head of chemical analysis group in the department IAM-AWP of KIT. We thank him for the composition.

Data Availability

The raw/processed data required to reproduce these findings cannot be shared at this time due to technical or time limitations.

References

1. Lindau, R.; Möslang, A.; Rieth, M.; Klimiankou, M.; Materna-Morris, E.; Alamo, A.; Tavassoli, A.-A.F.; Cayron, C.; Lancha, A.-M.; Fernandez, P.; et al. Present development status of EUROFER and ODS-EUROFER for application in blanket concepts. *Fusion Eng. Des.* **2005**, *75-79*, 989–996, doi:10.1016/j.fusengdes.2005.06.186.
2. Odette, G.R. Recent progress in developing and qualifying nanostructured ferritic alloys for advanced fission and fusion applications. *JOM* **2014**, *66*, 2427–2441, doi:10.1007/s11837-014-1207-5.
3. Lucon, E. Tensile and fracture toughness properties of EUROFER ODS (“EU Batch”-6mm Plate) in the unirradiated condition. *SCK· CEN Open Rep. BLG-1024* **2006**.
4. Ohtsuka, S.; Ukai, S.; Fujiwara, M. Nano-mesoscopic structural control in 9CrODS ferritic/martensitic steels. *J. Nucl. Mater.* **2006**, *351*, 241–246, doi:10.1016/j.jnucmat.2006.02.006.
5. Ukai, S.; Mizuta, S.; Fujiwara, M.; Okuda, T.; Kobayashi, T. Development of 9Cr-ODS martensitic steel claddings for fuel pins by means of ferrite to austenite phase transformation. *J. Nucl. Sci. Technol.* **2002**, *39*, 778–788, doi:10.1080/18811248.2002.9715260.
6. Ukai, S.; Ohtsuka, S.; Kaito, T.; Sakasegawa, H.; Chikata, N.; Hayashi, S.; Ohnuki, S. High-temperature strength characterization of advanced 9Cr-ODS ferritic steels. *Mater. Sci. Eng. A* **2009**, *510-511*, 115–120, doi:10.1016/j.msea.2008.04.126.
7. Yamamoto, M.; Ukai, S.; Hayashi, S.; Kaito, T.; Ohtsuka, S. Reverse phase transformation from α to γ in 9Cr-ODS ferritic steels. *J. Nucl. Mater.* **2011**, *417*, 237–240, doi:10.1016/j.jnucmat.2010.12.250.
8. Klimenkov, M.; Lindau, R.; Möslang, A. TEM study of internal oxidation in an ODS-Eurofer alloy. *J. Nucl. Mater.* **2009**, *386-388*, 557–560, doi:10.1016/j.jnucmat.2008.12.176.
9. Klimiankou, M.; Lindau, R.; Möslang, A. Direct correlation between morphology of (Fe,Cr)23C6 precipitates and impact behavior of ODS steels. *J. Nucl. Mater.* **2007**, *367–370, Part A*, 173–178, doi:10.1016/j.jnucmat.2007.03.150.
10. Mateus, R.; Carvalho, P.A.; Nunes, D.; Alves, L.C.; Franco, N.; Correia, J.B.; Alves, E. Microstructural characterization of the ODS Eurofer 97 EU-batch. *Fusion Eng. Des.* **2011**, *86*, 2386–2389, doi:10.1016/j.fusengdes.2011.01.011.

11. Zilnyk, K.D.; Oliveira, V.B.; Sandim, H.R.Z.; Möslang, A.; Raabe, D. Martensitic transformation in Eurofer-97 and ODS-Eurofer steels: A comparative study. *J. Nucl. Mater.* **2015**, *462*, 360–367, doi:10.1016/j.jnucmat.2014.12.112.

12. Chauhan, A.; Litvinov, D.; de Carlan, Y.; Aktaa, J. Study of the deformation and damage mechanisms of a 9Cr-ODS steel: Microstructure evolution and fracture characteristics. *Mater. Sci. Eng. A* **2016**, *658*, 123–134, doi:10.1016/j.msea.2016.01.109.

13. Oka, H.; Tanno, T.; Ohtsuka, S.; Yano, Y.; Uwaba, T.; Kaito, T.; Ohnuma, M. Effect of thermo-mechanical treatments on nano-structure of 9Cr-ODS steel. *Nucl. Mater. Energy* **2016**, *9*, 346–352, doi:10.1016/j.nme.2016.10.007.

14. Lindau, R.; Möslang, A.; Schirra, M.; Schlossmacher, P.; Klimenkov, M. Mechanical and microstructural properties of a hipped RAFM ODS-steel. *J. Nucl. Mater.* **2002**, *307–311, Part 1*, 769–772, doi:10.1016/S0022-3115(02)01045-0.

15. McClintock, D.A.; Sokolov, M.A.; Hoelzer, D.T.; Nanstad, R.K. Mechanical properties of irradiated ODS-EUROFER and nanocluster strengthened 14YWT. *J. Nucl. Mater.* **2009**, *392*, 353–359, doi:10.1016/j.jnucmat.2009.03.024.

16. Byun, T.S.; Yoon, J.H.; Hoelzer, D.T.; Lee, Y.B.; Kang, S.H.; Maloy, S.A. Process development for 9Cr nanostructured ferritic alloy (NFA) with high fracture toughness. *J. Nucl. Mater.* **2014**, *449*, 290–299, doi:10.1016/j.jnucmat.2013.10.007.

17. Byun, T.S.; Yoon, J.H.; Wee, S.H.; Hoelzer, D.T.; Maloy, S.A. Fracture behavior of 9Cr nanostructured ferritic alloy with improved fracture toughness. *J. Nucl. Mater.* **2014**, *449*, 39–48, doi:10.1016/j.jnucmat.2014.03.007.

18. Byun, T.S.; Hoelzer, D.T.; Kim, J.H.; Maloy, S.A. A comparative assessment of the fracture toughness behavior of ferritic-martensitic steels and nanostructured ferritic alloys. *J. Nucl. Mater.* **2017**, *484*, 157–167, doi:10.1016/j.jnucmat.2016.12.004.

19. Miyata, R.; Ukai, S.; Wu, X.; Oono, N.; Hayashi, S.; Ohtsuka, S.; Kaito, T. Strength correlation with residual ferrite fraction in 9CrODS ferritic steel. *J. Nucl. Mater.* **2013**, *442*, S138–S141, doi:10.1016/j.jnucmat.2013.04.086.

20. Yamamoto, M.; Ukai, S.; Hayashi, S.; Kaito, T.; Ohtsuka, S. Formation of residual ferrite in 9Cr-ODS ferritic steels. *Mater. Sci. Eng. A* **2010**, *527*, 4418–4423, doi:10.1016/j.msea.2010.03.079.

21. Pippan, R.; Hohenwarter, A. The importance of fracture toughness in ultrafine and nanocrystalline bulk materials. *Mater. Res. Lett.* **2016**, *4*, 127–136, doi:10.1080/21663831.2016.1166403.

22. Hohenwarter, A.; Pippan, R. Fracture of ECAP-deformed iron and the role of extrinsic toughening mechanisms. *Acta Mater.* **2013**, *61*, 2973–2983, doi:10.1016/j.actamat.2013.01.057.

23. Chaouadi, R.; Coen, G.; Lucon, E.; Massaut, V. Crack resistance behavior of ODS and standard 9%Cr-containing steels at high temperature. *J. Nucl. Mater.* **2010**, *403*, 15–18, doi:10.1016/j.jnucmat.2010.05.021.

24. Eiselt, C.C.; Klimenkov, M.; Lindau, R.; Möslang, A.; Sandim, H.R.Z.; Padilha, A.F.; Raabe, D. High-resolution transmission electron microscopy and electron backscatter diffraction in nanoscaled ferritic and ferritic–martensitic oxide dispersion strengthened–steels. *J. Nucl. Mater.* **2009**, *385*, 231–235, doi:10.1016/j.jnucmat.2008.11.029.

25. R. Lindau Private communication - Information on 9Cr ODS Eurofer steel 2018.

26. Wang, C.; Wang, M.; Shi, J.; Hui, W.; Dong, H. Effect of microstructural refinement on the toughness of low carbon martensitic steel. *Scr. Mater.* **2008**, *58*, 492–495, doi:10.1016/j.scriptamat.2007.10.053.

27. Morawiec, A. A program for refinement of lattice parameters based on multiple convergent-beam electron diffraction patterns. *J. Appl. Crystallogr.* **2007**, *40*, 618–622, doi:10.1107/S0021889807018262.

28. Arora, K.; Viehrig, H. Evaluation of the ASTM and ISO J initiation procedures by applying the unloading compliance technique to reactor pressure vessel steels. *J. Test. Eval.* **2011**, *39*, doi:10.1520/JTE103405.

29. ASTM Standard E1820-13 Standard test method for measurement of Fracture Toughness 2013.

30. Kim Wallin *Fracture toughness of engineering materials - Estimation and application*; EMAS Publishing, 2011; ISBN 0-9552994-6-2.

31. Doerner, M.F.; Nix, W.D. A method for interpreting the data from depth-sensing indentation instruments. *J. Mater. Res.* **1986**, *1*, 601–609, doi:10.1557/JMR.1986.0601.

32. Oliver, W.C.; Pharr, G.M. An improved technique for determining hardness and elastic modulus using load and displacement sensing indentation experiments. *J. Mater. Res.* **1992**, *7*, 1564–1583, doi:10.1557/JMR.1992.1564.

33. Oliver, W.C.; Pharr, G.M. Measurement of hardness and elastic modulus by instrumented indentation: Advances in understanding and refinements to methodology. *J. Mater. Res.* **2004**, *19*, 3–20, doi:10.1557/jmr.2004.19.1.3.

34. E. Lucon, A. Leenaers, W. Vandermeulen *Post irradiation examination of a thermo-mechanically improved version of EUROFER ODS (SCK CEN-BLG-1028)*; EFDA Long Term Programme Task TW5-TTMS-001 Deliverable D05; SCK CEN: Mol, Belgium, 2006; p. 35;

35. Das, A.; Chekhonin, P.; Altstadt, E.; Bergner, F.; Heintze, C.; Lindau, R. Microstructural characterization of inhomogeneity in 9Cr ODS EUROFER steel. *J. Nucl. Mater.* **2020**, *533*, 152083, doi:10.1016/j.jnucmat.2020.152083.

36. Heintze, C.; Bergner, F.; Ulbricht, A.; Hernández-Mayoral, M.; Keiderling, U.; Lindau, R.; Weissgärber, T. Microstructure of oxide dispersion strengthened Eurofer and iron–chromium alloys investigated by means of small-angle neutron scattering and transmission electron microscopy. *J. Nucl. Mater.* **2011**, *416*, 35–39, doi:10.1016/j.jnucmat.2010.11.102.

37. Heintze, C.; Bergner, F.; Akhmadaliev, S.; Altstadt, E. Ion irradiation combined with nanoindentation as a screening test procedure for irradiation hardening. *J. Nucl. Mater.* **2016**, *472*, 196–205, doi:10.1016/j.jnucmat.2015.07.023.

38. Lucon, E. Mechanical Properties of Two Improved Eurofer ODS Steels Before and After Low Dose Neutron Irradiation at 300 °C. *Fusion Sci. Technol.* **2009**, *56*, 289–294, doi:10.13182/FST09-A8916.

39. Zhang, Z.; Orlov, D.; Vajpai, S.K.; Tong, B.; Ameyama, K. Importance of Bimodal Structure Topology in the Control of Mechanical Properties of a Stainless Steel. *Adv. Eng. Mater.* **2015**, *17*, 791–795, doi:10.1002/adem.201400358.

40. Sekiguchi, T.; Ono, K.; Fujiwara, H.; Ameyama, K. New microstructure design for commercially pure titanium with outstanding mechanical properties by mechanical milling and hot roll sintering. *Mater. Trans.* **2010**, *51*, 39–45.

41. Fujiwara, H.; Akada, R.; Noro, A.; Yoshita, Y.; Ameyama, K. Enhanced mechanical properties of nano/meso hybrid structure materials produced by hot roll sintering process. *Mater. Trans.* **2008**, 0712100259–0712100259.

42. Orlov, D.; Fujiwara, H.; Ameyama, K. Obtaining copper with harmonic structure for the optimal balance of structure-performance relationship. *Mater. Trans.* **2013**, *54*, 1549–1553.

43. Fu, J.; Brouwer, J.C.; Hendrikx, R.W.A.; Richardson, I.M.; Hermans, M.J.M. Microstructure characterisation and mechanical properties of ODS Eurofer steel subject to designed heat treatments. *Mater. Sci. Eng. A* **2020**, *770*, 138568, doi:10.1016/j.msea.2019.138568.

44. Ohtsuka, S.; Ukai, S.; Fujiwara, M.; Kaito, T.; Narita, T. Improvement of 9Cr-ODS martensitic steel properties by controlling excess oxygen and titanium contents. *J. Nucl. Mater.* **2004**, *329-333*, 372–376, doi:10.1016/j.jnucmat.2004.04.043.

45. Ohtsuka, S.; Ukai, S.; Fujiwara, M.; Kaito, T.; Narita, T. Nano-structure control in ODS martensitic steels by means of selecting titanium and oxygen contents. *J. Phys. Chem. Solids* **2005**, *66*, 571–575, doi:10.1016/j.jpcs.2004.06.033.

46. Ukai, S.; Ohtsuka, S. Nano-mesoscopic structure control in 9Cr–ODS ferritic steels. *Energy Mater.* **2007**, *2*, 26–35, doi:10.1179/174892407X210357.

47. Zhou, X.; Li, C.; Yu, L.; Li, H.; Liu, Y. Effects of Ti addition on microstructure and mechanical property of spark-plasma-sintered transformable 9Cr-ODS steels. *Fusion Eng. Des.* **2018**, *135*, 88–94, doi:10.1016/j.fusengdes.2018.07.019.

48. Noh, S.; Choi, B.-K.; Han, C.-H.; Kang, S.H.; Jang, J.; Jeong, Y.-H.; Kim, T.K. Effects of heat treatments on microstructures and mechanical properties of dual phase ODS steels for high temperature strength. *Nucl. Eng. Technol.* **2013**, *45*, 821–826, doi:10.5516/NET.02.2013.529.

49. Tanno, T.; Ohtsuka, S.; Yano, Y.; Kaito, T.; Oba, Y.; Ohnuma, M.; Koyama, S.; Tanaka, K. Evaluation of mechanical properties and nano-meso structures of 9–11%Cr ODS steels. *J. Nucl. Mater.* **2013**, *440*, 568–574, doi:10.1016/j.jnucmat.2013.04.006.

50. Ukai, S.; Kaito, T.; Ohtsuka, S.; Narita, T.; Fujiwara, M.; Kobayashi, T. Production and properties of nano-scale oxide dispersion strengthened (ODS) 9Cr martensitic steel claddings. *ISIJ Int.* **2003**, *43*, 2038–2045.

51. Narita, T.; Ukai, S.; Ohtsuka, S.; Inoue, M. Effect of tungsten addition on microstructure and high temperature strength of 9CrODS ferritic steel. *J. Nucl. Mater.* **2011**, *417*, 158–161, doi:10.1016/j.jnucmat.2011.01.060.

52. Ohtsuka, S.; Ukai, S.; Sakasegawa, H.; Fujiwara, M.; Kaito, T.; Narita, T. Nano-mesoscopic structural characterization of 9Cr-ODS martensitic steel for improving creep strength. *J. Nucl. Mater.* **2007**, *367-370*, 160–165, doi:10.1016/j.jnucmat.2007.03.004.

53. Curry, D.A.; Knott, J.F. Effect of microstructure on cleavage fracture toughness of quenched and tempered steels. *Met. Sci.* **1979**, *13*, 341–345, doi:10.1179/msc.1979.13.6.341.

54. Yang, W.-J.; Lee, B.-S.; Oh, Y.-J.; Huh, M.-Y.; Hong, J.-H. Microstructural parameters governing cleavage fracture behaviors in the ductile–brittle transition region in reactor pressure vessel steels. *Mater. Sci. Eng. A* **2004**, *379*, 17–26, doi:10.1016/j.msea.2003.10.289.

55. Byun, T.S.; Kim, J.H.; Yoon, J.H.; Hoelzer, D.T. High temperature fracture characteristics of a nanostructured ferritic alloy (NFA). *J. Nucl. Mater.* **2010**, *407*, 78–82, doi:10.1016/j.jnucmat.2010.09.031.

56. Kim, J.H.; Byun, T.S.; Shin, E.; Seol, J.-B.; Young, S.; Reddy, N.S. Small angle neutron scattering analyses and high temperature mechanical properties of nano-structured oxide dispersion-strengthened steels produced via cryomilling. *J. Alloys Compd.* **2015**, *651*, 363–374, doi:10.1016/j.jallcom.2015.08.100.

57. Kim, J.H.; Byun, T.S.; Hoelzer, D.T. Tensile fracture characteristics of nanostructured ferritic alloy 14YWT. *J. Nucl. Mater.* **2010**, *407*, 143–150, doi:10.1016/j.jnucmat.2010.09.054.

58. Kim, J.H.; Byun, T.S.; Hoelzer, D.T. High temperature deformation mechanisms of nanostructured ferritic alloys in the context of internal variable theory of inelastic deformation. *J. Nucl. Mater.* **2013**, *442*, 458–462, doi:10.1016/j.jnucmat.2013.02.048.

59. Han Kim, J.; Sang Byun, T.; Hoelzer, D.T. Stress relaxation behavior of nanocluster-strengthened ferritic alloy at high temperatures. *J. Nucl. Mater.* **2012**, *425*, 147–155, doi:10.1016/j.jnucmat.2011.06.040.

60. Zhang, X.Z.; Knott, J.F. Cleavage fracture in bainitic and martensitic microstructures. *Acta Mater.* **1999**, *47*, 3483–3495.

61. Garrison, W.M.; Moody, N.R. Ductile fracture. *J. Phys. Chem. Solids* **1987**, *48*, 1035–1074, doi:10.1016/0022-3697(87)90118-1.

62. Pineau, A.; Benzerga, A.A.; Pardoen, T. Failure of metals I: Brittle and ductile fracture. *Acta Mater.* **2016**, *107*, 424–483, doi:10.1016/j.actamat.2015.12.034.

63. Lee, S.; Kim, S.; Hwang, B.; Lee, B.S.; Lee, C.G. Effect of carbide distribution on the fracture toughness in the transition temperature region of an SA 508 steel. *Acta Mater.* **2002**, *50*, 4755–4762.

64. Edelson, B.I.; Baldwin Jr, W.M. The effect of second phases on the mechanical properties of alloys. *Trans ASM* **1962**, *55*, 230–250.

65. Srivastava, A.; Ponson, L.; Osovski, S.; Bouchaud, E.; Tvergaard, V.; Needleman, A. Effect of inclusion density on ductile fracture toughness and roughness. *J. Mech. Phys. Solids* **2014**, *63*, 62–79, doi:10.1016/j.jmps.2013.10.003.

66. Gao, X.; Wang, T.; Kim, J. On ductile fracture initiation toughness: Effects of void volume fraction, void shape and void distribution. *Int. J. Solids Struct.* **2005**, *42*, 5097–5117, doi:10.1016/j.ijsolstr.2005.02.028.

67. Serrano, M.; García-Junceda, A.; Hernández, R.; Mayoral, M.H. On anisotropy of ferritic ODS alloys. *Mater. Sci. Technol.* **2014**, *30*, 1664–1668, doi:10.1179/1743284714Y.0000000552.

68. Chauhan, A.; Litvinov, D.; Aktaa, J. High temperature tensile properties and fracture characteristics of bimodal 12Cr-ODS steel. *J. Nucl. Mater.* **2016**, *468*, 1–8, doi:10.1016/j.jnucmat.2015.11.013.

69. Hadraba, H.; Fournier, B.; Stratil, L.; Malaplate, J.; Rouffié, A.-L.; Wident, P.; Ziolek, L.; Béchade, J.-L. Influence of microstructure on impact properties of 9–18%Cr ODS steels for fusion/fission applications. *J. Nucl. Mater.* **2011**, *411*, 112–118, doi:10.1016/j.jnucmat.2011.01.038.

70. Rouffié, A.L.; Wident, P.; Ziolek, L.; Delabrouille, F.; Tanguy, B.; Crépin, J.; Pineau, A.; Garat, V.; Fournier, B. Influences of process parameters and microstructure on the fracture mechanisms of ODS steels. *J. Nucl. Mater.* **2013**, *433*, 108–115, doi:10.1016/j.jnucmat.2012.08.050.

71. Chao, J.; Capdevila, C.; Serrano, M.; Garcia-Junceda, A.; Jimenez, J.A.; Pimentel, G.; Urones-Garrote, E. Notch impact behavior of oxide-dispersion-strengthened (ODS) Fe20Cr5Al alloy. *Metall. Mater. Trans. A* **2013**, *44*, 4581–4594, doi:10.1007/s11661-013-1815-7.

72. Das, A.; Viehrig, H.W.; Bergner, F.; Heintze, C.; Altstadt, E.; Hoffmann, J. Effect of microstructural anisotropy on fracture toughness of hot rolled 13Cr ODS steel – The role of primary and secondary cracking. *J. Nucl. Mater.* **2017**, *491*, 83–93, doi:10.1016/j.jnucmat.2017.04.059.

73. Kalyanam, S.; Beaudoin, A.J.; Dodds Jr., R.H.; Barlat, F. Delamination cracking in advanced aluminum–lithium alloys – Experimental and computational studies. *Eng. Fract. Mech.* **2009**, *76*, 2174–2191, doi:10.1016/j.engfracmech.2009.06.010.

74. Alam, M.E.; Pal, S.; Maloy, S.A.; Odette, G.R. On delamination toughening of a 14YWT nanostructured ferritic alloy. *Acta Mater.* **2017**, *136*, 61–73, doi:10.1016/j.actamat.2017.06.041.

75. Ritchie, R.O.; Thompson, A.W. On macroscopic and microscopic analyses for crack initiation and crack growth toughness in ductile alloys. *Metall. Trans. A* **1985**, *16*, 233–248.

76. Ritchie, R.O. The conflicts between strength and toughness. *Nat. Mater.* **2011**, *10*, 817–822, doi:10.1038/nmat3115.

77. Praud, M.; Mompiou, F.; Malaplate, J.; Caillard, D.; Garnier, J.; Steckmeyer, A.; Fournier, B. Study of the deformation mechanisms in a Fe–14% Cr ODS alloy. *J. Nucl. Mater.* **2012**, *428*, 90–97, doi:10.1016/j.jnucmat.2011.10.046.

78. Hoelzer, D.T.; Unocic, K.A.; Sokolov, M.A.; Byun, T.S. Influence of processing on the microstructure and mechanical properties of 14YWT. *J. Nucl. Mater.* **2016**, *471*, 251–265, doi:10.1016/j.jnucmat.2015.12.011.

79. Steckmeyer, A.; Praud, M.; Fournier, B.; Malaplate, J.; Garnier, J.; Béchade, J.L.; Tournié, I.; Tancray, A.; Bougault, A.; Bonnaillie, P. Tensile properties and deformation mechanisms of a 14Cr ODS ferritic steel. *J. Nucl. Mater.* **2010**, *405*, 95–100, doi:10.1016/j.jnucmat.2010.07.027.

80. Kimura, Y.; Inoue, T.; Yin, F.; Tsuzaki, K. Delamination toughening of ultrafine grain structure steels processed through tempforming at elevated temperatures. *ISIJ Int.* **2010**, *50*, 152–161, doi:10.2355/isijinternational.50.152.